APPLICATION OF PLASTIC-DAMAGE MULTIDIRECTIONAL FIXED SMEARED CRACK MODEL IN ANALYSIS OF RC STRUCTURES

A. Edalat-Behbahani*[1], J. A. O. Barros[1], A. Ventura-Gouveia[2]

[1]ISISE, Dep. Civil Eng., School of Engineering, University of Minho, Guimarães, Portugal

[2]ISISE, Dep. Civil Eng., School of Technology and Management of Viseu, Polytechnic Institute of Viseu, Viseu, Portugal

ABSTRACT

This paper describes a plasticity-damage multidirectional fixed smeared cracking (PDSC) model to simulate the failure process of concrete and reinforced concrete (RC) structures subjected to different loading paths. The model proposes a unified approach combining a multidirectional fixed smeared crack model to simulate the crack initiation and propagation with a plastic-damage model to account for the inelastic compressive behaviour of concrete between cracks. The smeared crack model considers the possibility of forming several cracks in the same integration point during the cracking process. The plasticity part accounts for the development of irreversible strains and volumetric strain in compression, whereas the strain softening and stiffness degradation of the material under compression are controlled by an isotropic strain base damage model. The theoretical aspects about coupling the fracture, plasticity, and damage components of the model, as well as the model appraisal at both material and structural levels, have been detailed in a former publication. This study briefly summarizes the model formulations, and is mainly dedicated to further explore the potentialities of the proposed constitutive model for the analysis of concrete and RC structures. The model is employed to simulate experimental tests that are governed by nonlinear phenomenon due to simultaneous occurrence of cracking and inelastic deformation in compression. The numerical simulations have predicted with good accuracy the load carrying capacity, ductility, crack pattern, plastic (compressive) zone, and failure modes of all types of structures analysed. The influence of the model parameters that simulate the nonlinear behaviour of concrete under tension and compression is analysed through a parametric study.

KEYWORDS: Finite element analysis, Constitutive model, Compressive nonlinearity, Cracked concrete, RC structures.

* Author to whom correspondence should be send (aliedalatbehbahani@gmail.com)

1. INTRODUCTION

Nonlinear finite element analysis (NFEA) has now been widely adopted as an effective and reliable method to analyze reinforced concrete (RC) structures subjected to various loading scenarios. Amongst many key factors that affect the reliability of a NFEA tool used for analysing RC structures, the selected constitutive model still remains the foremost challenging task due to the complexity of concrete behaviour. Concrete exhibits highly nonlinear behaviour by increasing deformation, with dissymmetric responses in tension and in compression. Experimental tests demonstrate that concrete behaviour in tension is brittle, and after cracking initiation concrete develops a softening behaviour with a decay of tensile capacity with the widening of the cracks. This crack opening process is followed by a decrease of crack shear stress transfer due to the deterioration of aggregate interlock. Concrete in compression also demonstrates a pronounced nonlinear behaviour with an inelastic irreversible deformation. In the pre-peak stage of concrete response in uniaxial compression, a nonlinear stage is observed, whose amplitude depends of the concrete strength class, followed by a softening stage where brittleness is also dependent of the strength class. For a realistic NFEA of RC structures, constitutive models are required to adequately describe these complex behaviours of concrete.

This study is mainly dedicated to evaluate the potentialities of a plastic-damage multidirectional smeared crack constitutive model able to represent the complex failure mechanism of concrete in tension and compression. The proposed model simulates the crack opening and shear sliding according to an already existing multidirectional fixed smeared crack model [1–3]. The models based on a smeared crack approach assume that the local displacement discontinuities at cracks are distributed, theoretically, over a certain length used to transform crack width/sliding in a strain concept, also assumed to represent the length zone of the fracture process [4-5]. This length dimension is related to the finite element characteristics in order to assure the results are independent of the adopted finite element mesh refinement, preserving the fracture energy as a material property. However, these models cannot predict the precise localization and propagation of the discrete cracks, since the assumption of continuity of displacement field does not reflect the nature of displacement discontinuities at the cracks. However the smeared cracking approach is very convenient for relatively large concrete structures, mainly those with reinforcement that assure the formation of relatively high number of cracks, since modelling the cracking process is almost resumed to the adoption of a proper constitutive model.

The proposed model simulates the inelastic compressive behaviour of the material between cracks by a numerical strategy that combines plasticity and damage theories. The theory of plasticity has been frequently used for modelling compression due to its simple and direct representation of multiaxial stress field. The models based on the theory of plasticity are able to describe the dilatancy, permanent strain and hardening/softening behaviour of the concrete, see for instance [6-9], but the experimentally observed stiffness degradation of concrete is not captured accurately by using exclusively the plasticity theory [10, 11]. On the other hand, the theoretical framework of the continuum damage

mechanics (CDM) is based on the gradual reduction of the elastic stiffness. The damage is defined as the loss of strength and stiffness of the material when subjected to a certain loading process. However the CDM alone is not able to reproduce the irreversible (permanent) deformation of the concrete that is pronounced when highly confined [12-14].

So, in the proposed model, plasticity and damage theories are being merged in an attempt of constituting reliable approaches capable of simulating the strength and stiffness degradation and occurrence of irreversible deformations of concrete in compression. Combination of the plasticity and damage theories is assured by considering the plastic flow occurs in undamaged (with respect to compression) material, together with the strain based damage approach assuming state of damage equally distributed in all the material directions (isotropic damage).

Formulation of the constitutive model, as well as the theoretical consideration for coupling the smeared cracking, plasticity, and damage concepts of the model are detailed in a previous publication [15]. The former studies [15-16] include also the implementation of the proposed constitutive model into FEMIX FEM based computer program [17], and the model appraisal at both material and structural levels. The present paper includes a short resume of the model formulation, and mainly discusses the capabilities of the model for simulating the behaviour of concrete and RC structures whose failure is governed by cracking and inelastic behaviour in compression. In this type of simulations the concrete of a large number of integration points (IP) is submitted to cracking and inelastic compressive deformations. This situation can be considered as a complicated loading scenario, since both smeared cracking and plastic-damage parts of the model are active over a large region of the simulated structure, therefore two types of nonlinearities are occurring simultaneously. A wide range of experimental tests including splitting tensile test, RC deep beams with square openings, and a series of RC shear wall panels submitted to biaxial loading conditions, are simulated to highlight the capability of the model to simulate the behaviour of this type of structures with good accuracy. For all the analysis the results are compared with the experimental observations. The paper ends with a parametric study that aims to highlight the sensitivity of the numerical simulations to the values adopted for the model parameters.

2. MODEL DESCRIPTION

2.1 Introduction

This section describes briefly the formulation of the plastic-damage multidirectional smeared crack (PDSC) constitutive model, since a detailed exposition can be found elsewhere [15].

2.2 Plastic-damage multidirectional fixed smeared crack (PDSC) model

Modelling cracked materials using a smeared approach is usually based on the decomposition of the total incremental strain vector, $\Delta\underline{\varepsilon}$, into an incremental crack strain vector, $\Delta\underline{\varepsilon}^{cr}$, and an incremental concrete strain vector, $\Delta\underline{\varepsilon}^{co}$, as

proposed by de Borst and Nauta [18], ($\Delta\underline{\varepsilon} = \Delta\underline{\varepsilon}^{co} + \Delta\underline{\varepsilon}^{cr}$). Deformational contribution of the sets of smeared cracks that can be formed (according to a crack opening criterion) in an integration point (IP) is considered in $\Delta\underline{\varepsilon}^{cr}$. For modelling a cracked member with material between cracks in nonlinear compression, the term $\Delta\underline{\varepsilon}^{co}$ is further decomposed into its elastic ($\Delta\underline{\varepsilon}^{e}$) and plastic parts ($\Delta\underline{\varepsilon}^{p}$), ($\Delta\underline{\varepsilon}^{co} = \Delta\underline{\varepsilon}^{e} + \Delta\underline{\varepsilon}^{p}$). Thereby the incremental constitutive relation of the PDSC model is obtained as:

$$\Delta\underline{\bar{\sigma}} = \underline{D}^{e} (\Delta\underline{\varepsilon} - \Delta\underline{\varepsilon}^{p} - \Delta\underline{\varepsilon}^{cr}) \quad (1)$$

being $\Delta\underline{\bar{\sigma}} = \{\Delta\bar{\sigma}_1, \Delta\bar{\sigma}_2, \Delta\bar{\tau}_{12}\}$ the incremental stress vector induced in the material due to $\Delta\underline{\varepsilon} = \{\Delta\varepsilon_1, \Delta\varepsilon_2, \Delta\gamma_{12}\}$, and considering the constitutive matrix of the intact material, $\underline{D}^{e}$.

The $\Delta\underline{\varepsilon}^{cr}$ is evaluated using a multidirectional fixed smeared crack model [1-3] that considers the possibility of forming several cracks in the same IP, whose orientations, conditioned by an adopted criterion, are however preserved constant during the cracking process. The crack initiation is governed by the Rankine failure criterion that assumes a crack occurs when the maximum principal tensile stress in an IP attains the concrete tensile strength (f_{ct}) under an assumed tolerance. After crack initiation, the relationship between the normal stress and the normal strain in the crack coordinate system, i.e. $\sigma_n^{cr} - \varepsilon_n^{cr}$, is simulated via the trilinear diagram represented in Fig. 1 [1]. Normalized strain, $\xi_i\ (i = 1,2)$, and stress, $\alpha_i\ (i = 1,2)$, parameters are used to define the transition points between linear segments, being G_f^{I} the fracture energy mode I, while l_b is the characteristic length (crack bandwidth) used to assure that the results of a material nonlinear analysis is not dependent of the refinement of the finite element mesh.

The model simulates the shear behaviour of the cracked concrete using an incremental crack shear stress-shear strain approach based on a shear retention factor. According to this approach, the crack shear stress (τ_t^{cr}) increases with the crack shear strain (γ_t^{cr}) up to attain a maximum that depends on the crack shear modulus (D_t^{cr}), see Fig. 2 [19]. The modulus D_t^{cr} is simulated as [1]:

$$D_t^{cr} = \frac{\beta}{1-\beta} G_c \quad (2)$$

where G_c is the concrete elastic shear modulus, while the shear retention factor, β , can be a constant value or, alternatively, a function of current crack normal strain, ε_n^{cr} , and of ultimate crack normal strain, $\varepsilon_{n,u}^{cr}$, such as:

$$\beta = \left(1 - \frac{\varepsilon_n^{cr}}{\varepsilon_{n,u}^{cr}}\right)^{P_1} \quad (3)$$

being the exponent P_1 a parameter that defines the decrease rate of β with increasing ε_n^{cr} .

The plastic strain vector, $\Delta\underline{\varepsilon}^{p}$, which appears in Eq. (1), includes the inelastic compressive deformation of the material between the smeared cracks. The plastic strain vector is evaluated by a stress based plasticity model according to the following flow rule:

$$\Delta\underline{\varepsilon}^{p} = \Delta\lambda \frac{\partial f}{\partial \underline{\bar{\sigma}}} \tag{4}$$

where $\Delta\lambda$ is the non-negative plastic multiplier and f is a scalar function, called yield function, that is dependent on the stress vector $\underline{\bar{\sigma}}$ applied to the undamaged (with respect to compression) configuration of the material, and the hardening function $\bar{\sigma}_c$, i.e. $f = f(\underline{\bar{\sigma}}; \bar{\sigma}_c)$. The yield function, f, was derived from the five-parameter Willam and Warnke failure criterion [20] (the details of this process are in the [15]). The equation of this yield function is [15]:

$$f\left(\underline{\bar{\sigma}}; \bar{\sigma}_c(\tilde{\epsilon}_c)\right) = \left[\left(\frac{\bar{I}_1}{\sqrt{3}c} - \frac{\sqrt{2}\,b}{c}\sqrt{\bar{J}_2}\right)\bar{\sigma}_c(\tilde{\epsilon}_c) - \frac{2a}{c}\bar{J}_2\right]^{1/2} - \bar{\sigma}_c(\tilde{\epsilon}_c) = 0 \tag{5}$$

where $\bar{I}_1$ is the first invariant of the stress tensor, $\bar{J}_2$ is the second invariant of the deviatoric stress tensor:

$$\bar{I}_1 = \underline{\bar{\sigma}}_{ii}; \quad \bar{J}_2 = \tfrac{1}{2}\underline{\bar{S}}_{ij}\underline{\bar{S}}_{ij} \tag{6}$$

where $\underline{\bar{\sigma}}_{ij,(i,j=1,2,3)}$ is the stress tensor, $\underline{\bar{S}}_{ij} = \underline{\bar{\sigma}}_{ij} - \underline{\delta}_{ij}\bar{I}_1/3$ is the deviatoric stress tensor. The variables *a*, *b* and *c* are the scalars used to interpolate the current yield meridian between the tensile meridian and compressive meridian, as described in detail in Edalat-Behbahani et al., [15].

Hardening function ($\bar{\sigma}_c$) carries the meaning of uniaxial compressive stress acting on undamaged (with respect to compression) configuration of the material, and is dependent on the hardening parameter ($\tilde{\epsilon}_c$). The hardening parameter is a scalar measure used to characterize the plastic state of the material under compressive stress field. In fact, the compressive behaviour of the material is governed by the uniaxial hardening law $\bar{\sigma}_c - \tilde{\epsilon}_c$ represented in Fig. 3a. In this figure f_c is the compressive strength, and f_{c0} is the uniaxial compression stress at the initiation of the stress-strain nonlinear behaviour, defined by the α_0 that is a material constant in the range $]0,1[$ i.e. $f_{c0} = \bar{\sigma}_c(\tilde{\epsilon}_c = 0) = \alpha_0 f_c$. Hardening parameter at the compressive strength ($\tilde{\epsilon}_{c1}$) is obtained from the following equation:

$$\tilde{\epsilon}_{c1} = \varepsilon_{c1} - f_c/E \tag{7}$$

being ε_{c1} the strain at compressive strength, and E is the elasticity modulus of concrete.

Once the $\Delta\underline{\bar{\sigma}}$ is calculated from Eq. (1) at a generic $n+1$ loading stage ($\Delta\underline{\bar{\sigma}}_{n+1}$), the stress vector at this stage is updated ($\underline{\bar{\sigma}}_{n+1} = \underline{\bar{\sigma}}_n + \Delta\underline{\bar{\sigma}}_{n+1}$). The stress vector $\underline{\bar{\sigma}}_{n+1}$ does not take into account the strain softening of the material under compression since the adopted $\bar{\sigma}_c - \tilde{\epsilon}_c$ law (Fig. 3a) at the post-peak stage ($\tilde{\epsilon}_c > \tilde{\epsilon}_{c1}$) does not include a softening

branch (slop of the $\bar{\sigma}_c - \tilde{\epsilon}_c$ law for the domain $\tilde{\epsilon}_c > \tilde{\epsilon}_{c1}$ is zero). To simulate the strain softening and stiffness degradation of the material under compression, an isotropic damage law is included according to the following equation [15]:

$$\underline{\sigma}_{n+1} = \underline{\bar{\sigma}}^{+}_{n+1} + (1 - d_{c,n+1})\,\underline{\bar{\sigma}}^{-}_{n+1} \tag{8}$$

where $\underline{\sigma}_{n+1}$ is the stress vector in damaged (with respect to compression) configuration of the material, $\underline{\bar{\sigma}}^{+}_{n+1}$ and $\underline{\bar{\sigma}}^{-}_{n+1}$ are the positive (tensile) and the negative (compressive) parts of the stress vector $\underline{\bar{\sigma}}_{n+1}$. The variable d_c is a scalar measure in the range $[0,1]$ that is used to represent the damage level due to compression. Fig. 3(b) represents the evolution of the variable d_c as a function of a scalar parameter known as damage internal variable, $\tilde{\epsilon}_d$. The variable $\tilde{\epsilon}_d$ can be evaluated as a function of the plasticity hardening variable, $\tilde{\epsilon}_c$, according to the following equation [15]:

$$\tilde{\epsilon}_d = \begin{cases} 0 & if\ \tilde{\epsilon}_c \le \tilde{\epsilon}_{c1} \\ \tilde{\epsilon}_c - \tilde{\epsilon}_{c1} & if\ \tilde{\epsilon}_c > \tilde{\epsilon}_{c1} \end{cases} \tag{9}$$

Analysis of Fig. 3(b) indicates that at the plastic deformation corresponding to $\tilde{\epsilon}_c \le \tilde{\epsilon}_{c1}$ ($\tilde{\epsilon}_d = 0$) the material is intact ($d_c = 0$), and for $\tilde{\epsilon}_c = \tilde{\epsilon}_{cu}$ ($\tilde{\epsilon}_d = \tilde{\epsilon}_{cu} - \tilde{\epsilon}_{c1}$) the material is completely damaged ($d_c = 1$). The variable $\tilde{\epsilon}_{cu}$ is the maximum equivalent strain in compression that is related to the compressive fracture energy ($G_{f,c}$), the characteristic length for compression (l_c), the compressive strength (f_c), and $\tilde{\epsilon}_{c1}$ according to the following equation [15] (see Fig. 3(b) and Fig. 3(c)):

$$\tilde{\epsilon}_{cu} = \frac{3.1\,G_{f,c}}{l_c\,f_c} - \frac{11}{48}\tilde{\epsilon}_{c1} \tag{10}$$

The characteristic lengths in tension (l_b) and compression (l_c) are usually considered the same [21], then in the present approach $l_c = l_b$. The parameters α_0, f_c, ε_{c1}, $G_{f,c}$ can be determined by the stress-strain response (let's designate this response as $\sigma_c - \varepsilon_c$) obtained from compression tests carried out in high stiff rigs, under displacement control, with specimens of slenderness capable of assuring a central zone considered in uniaxial stress field (for this purpose is opportune to minimize friction between the specimen extremities and the loading platens of the testing rig), where the strains are locally measured up to the complete exhaustion of the load carrying capacity of the model. For plain concrete, CEB-FIP Model Code 2010 [22] has recommendations to derive E, α_0, ε_{c1}, $G_{f,c}$ from f_c (it is assumed the same E in compression and tension).

3. PREDICTIVE PERFORMANCE OF THE MODEL

3.1 Introduction

The PDSC model was implemented in FEMIX 4.0 computer program [17] as a new approach to simulate the nonlinear behaviour of concrete and RC structures. This section is dedicated to assess the model robustness and predictive performance when applied to different types of concrete and RC structures. Several experimental tests from literature including splitting tensile test, RC deep beams with square openings, RC shear walls submitted to biaxial loading conditions are simulated, and comparisons with available experimental data are executed. These structures are of particular interest for the assessment of the reliability of the proposed model, since in these examples the failure mechanism involved simultaneous occurrence of cracking and inelastic deformation in compression. The structures under consideration are also simulated by another constitutive model, available in FEMIX 4.0, which includes the same multidirectional fixed smeared crack approach [1-3] to account for cracking, but considers the linear elastic behaviour for the material under compressive deformations. The later model is herein designated as SC model.

For all the analysis performed in this study, the incremental-iterative procedure is used in the form of a modified Newton Raphson method, where the tangential stiffness matrix is only updated in the first iteration of each load increment. The convergence criterion is based on the normalized energy norm assuming an error tolerance of 0.001. A path independent approach was adopted for the stress update strategy in the incremental-iterative procedure. The numerical simulations are executed in displacement control in order to reproduce, as much as possible, the experimental testing conditions. The analysis is interrupted when the crack pattern demonstrates the eminence of structural collapse, which is in general followed by difficulties in assuring convergence due to the formation of failure mechanisms.

3.2 Indirect (splitting) tensile test

Splitting tensile tests are frequently executed as the indirect method for determining the tensile strength of cement based materials. In this section the model ability to predict the concrete behaviour under the splitting tensile test is investigated. The model is applied to simulate the test executed in the work of Abrishambaf et al. [23], and the model predictions are compared with the results reported at the experimental program. The specimen is a cylinder with a diameter of 150 mm and length of 60 mm made by a steel fibre reinforced self-compacting concrete, SFRSCC, of 60 kg per m^3 steel fibers. To localize the crack plane, the specimen includes two 5 mm notches cut on each opposite face of the specimen. Fig. 4 shows the specimen geometry, loading configuration and experimental crack pattern observed at the failure stage.

Only a quarter of the specimen is modelled, due to the double symmetry condition. Roller supports were imposed at all the nodes on the both axes of symmetry to fix the displacements perpendicular to the axes of symmetry (see Fig. 5). The finite element mesh of 8-noded plane stress finite elements with 3×3 Gauss-Legendre IP scheme was adopted for the specimen and the loading plate, see Fig. 5. Elements of the loading plate are assumed to exhibit linear elastic behaviour

with the elastic modulus and Poisson's ratio corresponding to $E = 200$ GPa, and $\nu = 0.3$. Perfect bond was assumed between the elements of the loading plate and the elements of surrounding concrete. The applied load is uniformly distributed over the edges of the elements of the loading plate, under the displacement control by the arc-length method. The properties of concrete are taken from Abrishambaf et al. [23], and the values of the parameters to define the constitutive law for concrete are included in Table 1.

Fig. 6 demonstrates the applied load vs. the crack opening mouth displacement ($F-W$) response obtained at the experiment and the responses predicted by both SC and PDSC constitutive models. The good predictive performance of the PDSC model is further demonstrated by providing the numerical crack pattern and the plastic zone i.e. the area indicating those IPs under inelastic compressive deformation, obtained at the final converged loading step of the calculation process (see Fig. 7).

The analysis executed by SC model reveals at the load corresponding to ≈ 45 kN the splitting cracks are initiated (see Fig. 6). These cracks have an orientation of $\theta \approx 0^{o}$ and are formed in IPs in the vicinity of the vertical symmetry axis of the cylinder. Once these cracks start to propagate ($W > 0$), the stiffness of $F-W$ response slightly decreases, but the predicted load carrying capacity continuously increases without the occurrence of a failure load, since this model (SC model) assumes an elastic behaviour for the concrete in compression. However according to the PDSC response, after the initiation of the splitting cracks ($W > 0$), the predicted load increases and attains a hardening branch followed by a softening stage that is mainly governed by the nonlinear inelastic behaviour of concrete under compression. From Fig. 6 it is evident that there is a close correlation between the experimental $F-W$ response and the one predicted by the PDSC model. Fig. 7(a) demonstrates that the cracks having the orientation of $\theta \approx 0^{o}$ and with highly propagated opening status are spread along the vertical symmetry axis of the specimen, while Fig. 7(b) shows the plastic zone is concentrated at the region under the loading plate. These observations imply the final failure mechanism of this test (see Fig. 4(c)) is a combination of the tensile splitting crack and the compressive failure modes. The information required to interpret status of a generic crack at any stage of its development is indicated in the caption of the Fig. 7.

It should be aware that in the approach followed in the current work for modelling the behaviour of SFRSCC, this material is considered to be homogeneous. However SFRSCC can be regarded as a heterogeneous medium, like the approach proposed by Cunha et al. [26]. Within their numerical model, SFRSCC was modeled as a material composed of two phases: matrix and discrete steel fibres. The matrix phase is simulated with a 3D multidirectional fixed smeared crack model, while the stress transfer between crack planes due to the reinforcing mechanisms of fibres bridging active cracks is modeled with 3D embedded elements. This approach is, however, too demanding in terms of computer time consuming when applied to elements of structural scale, which is the type of structures aimed to be analyzed in the present work.

3.3 RC deep beams

Application of the PDSC model for simulating reinforced concrete deep beams with openings, tested by El-Maaddawy and Sherif [27], is considered in this section. A total of six beams (NS-200-B, NS-250-B, NS-200-T, NS-250-T, NS-200-C, NS-250-C) are analysed which have the same shear span over dept ratio, thickness, and reinforcement layout. All the beams include two square openings, one in each shear span, while the differences between these beams are restricted to the location and size of the openings. These beams can be categorized considering the location of the openings within shear span in three groups: *group C* which includes the beams whose openings are installed at the middle points of the shear spans; *group B*, and *group T*, which include the beams that their openings are located, respectively, at bottom of shear spans near loading points, and at top of the shear spans near supports. The opening size for each beam was either 200×200 mm^2 or 250×250 mm^2 giving the opening height over the depth (a/h) ratios of 0.4 and 0.5 respectively. More details corresponding to the geometry and loading configuration of these beams are provided at Fig. 8, and Table 2.

The tensile reinforcement consists of 4 steel bars of 14 mm diameter, with the cross-sectional area of 153.9 mm^2 for each bar, while two steel bar of 8 mm diameter, with the cross-section area of 50.3 mm^2 for each bar, are applied as the compressive reinforcement. The web reinforcements are applied with the steel bar of 6 mm diameter, with the cross-section area of 28.3 mm^2, spaced at 150 mm in both vertical and horizontal directions (see Fig. 8). The web reinforcement intersecting the opening spaces is cut prior to casting the corresponding specimen [27].

Due to symmetry of the beams about the vertical axis at the center of the beam, only half beam was modelled. Horizontal displacements of all the nodes on the symmetry axis of the beam are fixed, by applying roller support, to impose the symmetry condition. Eight-noded serendipity plane stress finite elements with 3×3 Gauss–Legendre IP scheme were used for modelling the beams, supports and loading plates. In Fig. 9 is represented, as an example, the finite element mesh used for the simulation of the beam NS-200-C. The steel reinforcement is meshed using 2-noded perfect bonded embedded cables with two IPs. The assumption of the perfect bond for the embedded cable elements implies the translational degrees of freedom of the nodes of these elements are constrained with respect to their host elements (plane stress finite elements used for modelling concrete). For modelling the behaviour of the steel bar elements, the stress-strain relationship represented in Fig. 10 was adopted. The curve (under compressive or tensile loading) is defined by the points PT1 = ($\varepsilon_{sy}, \sigma_{sy}$), PT2 = ($\varepsilon_{sh}, \sigma_{sh}$), and PT3 = ($\varepsilon_{su}, \sigma_{su}$) and a parameter P_2 that defines the shape of the last branch of the curve. Unloading and reloading linear branches with the slope of $E_s = \sigma_{sy} / \varepsilon_{sy}$ are assumed in the present approach [1]. The values of parameters used to define the stress-strain diagram indicated in Fig. 10 are included in Table 3. Support and loading plates are modeled as a linear-elastic material with

Poisson's coefficient of 0.3 and elasticity modulus of 200 GPa. Perfect bond was assumed between the elements of supports/loading plates and the elements of surrounding concrete. Properties of concrete are taken from Hawileh et al. [28], and the values of the parameters to define the PDSC model are, accordingly, included in Table 1.

Fig. 11 shows the experimental load vs. mid-span deflection ($P-U$ relationship) for the beams in analysis and the respective numerical predictions with the SC and PDSC models. Table 2 gives the failure loads of the beams obtained in the experimental program ($P_u^{\exp}$) and in the numerical simulations (P_u^{num}). Amongst the beams with the opening size of 200×200 mm^2 (NS-200-B, NS-200-T, NS-200-C), i.e. the beams having the *a/h* ratio of 0.4, the beam NS-200-T has the maximum experimental failure load (see Fig. 11 and Table 2). The failure load of the beam NS-200-T is close to that of the beam NS-200-B (the load corresponding to the beam NS-200-T is 4.4% larger than that of NS-200-B), and is 35% higher than that of the beam NS-200-C. The beam NS-200-C has the minimum failure load among these three beams, since its openings, located at the center of the shear spans, significantly interrupts the loading path which is a line connecting loading to the support plates. In case of the beams NS-200-B and NS-200-T whose openings are located at the corners of the shear spans, the loading paths are less interrupted and higher load carrying capacities are obtained at the experimental program. A close inspection of Table 2 also reveals that the PDSC model was able to simulate this experimental observation, since the numerical failure load (P_u^{num}) predicted for the beam NS-200-B is higher than that of NS-200-C and is lower than the value calculated for the beam NS-200-T.

By comparing the experimental failure loads of the beams in the same geometry group (*group B*, *group C*, or *group T*) but with the different opening sizes (different *a/h* ratios of 0.4 or 0.5), e.g. compare the failure load of the beam NS-200-T with that of the beam NS-250-T, it can be concluded as the opening size increases, the loading path of the beam is more interrupted, and the failure load decreases. From Fig. 11 and Table 2, it is evident that PDSC model was able to simulate the reduction of the load carrying capacity as the *a/h* ratio of the beams increases from 0.4 to 0.5.

Fig. 11 also shows that the PDSC model fit with high accuracy the experimental $P-U$ curves at all stages of loading till failure. The failure loads were predicted with the average error of 4.45% (see Table 2). If SC approach is taken into account to simulate these beams, the predicted $P-U$ responses consider the stiffness degradation only due to cracking of concrete and yielding of steel reinforcements. Since the SC model assumes a linear behaviour for the concrete in compression, the stiffness and ultimate load is overestimated for all the beams, and the final failure mode is incorrectly predicted as yielding of reinforcement (see Fig. 11).

The experimental cracking patterns of all the beams at the failure stage demonstrated two critical diagonal cracks in the above and below of one of the openings, see Fig. 12. As can be seen in Fig. 13, the crack patterns predicted by PDSC model demonstrate flexural cracks with insignificant opening status in middle of the beams, whereas more propagated diagonal cracks (cracks with the orientation of $\theta \approx 45^{\circ}$) can be observed along the line connecting the support and

loading plates. It seems clear that the PDSC model was able to simulate with high accuracy the experimentally observed crack patterns of the beams in analysis. The simulated plastic zones for these beam, see Fig. 13, evidence formation of the compressive struts connecting the loading points and supports.

3.4 Shear RC walls

To highlight the efficiency of the proposed constitutive model, the shear wall panels, tested by Maier and Thürlimann [29], were simulated. The analysed specimens are registered at the experiment as S1, S2, S3, S4, S9, and S10. The experimental loading procedure introduces an initial vertical compressive force, F_v, and then a horizontal force, F_h, that was increased up to the failure of the wall. These shear walls had a relatively thick beam at their bottom and top edges for fixing the walls to the foundation, and for applying F_h and F_v, respectively, as depicted in Fig. 14. The analysed shear walls differ in geometry, reinforcement ratio, and initial vertical load (F_v). These walls can be categorized considering geometry of the walls in two groups: *group A*, which includes walls with vertical flanges at their lateral edges; *group B*, which contains the walls with uniform rectangular cross section (without vertical flanges). All the walls are reinforced in both vertical and horizontal directions with the reinforcement ratios designated as ρ_x and ρ_y. For the walls at the *group A* (specimens with vertical flanges), ρ_F indicates the reinforcement ratio of the vertical flanges. Table 4 includes the details corresponding to geometry, reinforcement ratios, and initial vertical force for each shear wall analysed at this study.

FEM modelling of the walls and top beams were performed using 8-noded serendipity plane stress finite elements with 3×3 Gauss-Legendre IP scheme. Fig. 15(a) presents, as an example, the finite element mesh used for analysis of the wall S3. Instead of modelling the foundation, the bottom nodes of the panels are fixed in vertical and horizontal directions. The vertical and horizontal loads are uniformly distributed over the edges of the top beam, as schematically represented in Fig. 15(a). Elements of the top beam are assumed to exhibit linear elastic behaviour during the analysis, since no damage is reported for these elements in the original papers. For modelling the behaviour of the steel bars, the stress-strain relationship represented in Fig. 10 was adopted. The reinforcement is meshed using 2-noded perfect bonded embedded cables with two IPs. The values of parameters used to define the constitutive models of concrete and steel are included in Table 1 and Table 5, respectively. The effect of tension-stiffening was indirectly simulated using the trilinear tension-softening diagram.

The experimental relationship between the applied horizontal force and the horizontal displacement of the top beam, F_h-U_h, for the wall S3 is represented in Fig. 15(b). This figure also includes the predicted F_h-U_h response obtained by both PDSC and SC models. According to the experimental observations the wall S3 attains the load carrying capacity at peak stage corresponding to 977 kN, which is maximum amongst all the panels, and after attaining the peak the panel failed

in brittle manner mainly due to crushing of concrete at the bottom left side of the panel. At the failure stage, this panel is densely cracked as can be seen in the experimental crack pattern (see fig. 15(e)). Predictions of the PDSC model are obtained for three levels of compressive fracture energy ($G_{f,c} = 20, 30, 40\, N/mm$) to demonstrate the effect of this model parameter on behaviour of the simulated wall. At $U_h \approx 5\, mm$ the IP closest to the left bottom side of the wall enters in the compressive softening phase ($d_c > 0$). After $U_h \approx 10\, mm$ the load carrying capacity and ductility of the simulated F_h-U_h responses are significantly affected by changing the compressive fracture energy; the load carrying capacity and ductility increase with $G_{f,c}$. Ductility of the wall is underestimated for the simulation with $G_{f,c} = 20\, N/mm$, and overestimated when using $G_{f,c} = 40\, N/mm$. A proper fit of the experimentally observed load carrying capacity and ductility of F_h-U_h response was obtained for the simulation using $G_{f,c} = 30\, N/mm$. This value is close to the upper limit of the interval values obtained by Vonk [30]. Fig. 15(c) and (d) present, respectively, the numerical crack pattern and the plastic zone for the simulation using $G_{f,c} = 30\, N/mm$, at the deformation corresponding to $U_h \approx 16.5\, mm$ (final converged step). Fig. 15(c) demonstrates that the cracks with fully opened status are spread over a large area of the panel. The cracks at the right side of the panel (mainly at the right vertical flange of the panel) are mostly oriented with an inclination of about $\theta \approx 90^o$, while the cracks at the middle region of the panel have the orientation of $\theta \approx 45^o$. This numerical prediction correlates well with the experimental crack pattern (see Fig. 15(e)). The simulated plastic zone evidences the formation of a compressive strut connecting the right top side of the panel to the bottom left side.

Results of the analysis for the other shear walls are represented in Fig. 16 in terms of F_h-U_h relationship and crack pattern. As can be seen in this figure the PDSC model assuming $G_{f,c} = 30\, N/mm$ was able to accurately predict the overall experimental F_h-U_h behaviour and the experimental crack patterns of these walls. For all the 6 shear walls the numerical peak load, $F_{h,u}^{num}$, predicted by the PDSC model are compared with the experimental ones, $F_{h,u}^{\exp}$, at Table 4. The information provided at Table 4 verifies the peak loads of all the shear walls are precisely simulated with the average error of 4.85%. Comparing the F_h-U_h responses obtained by both PDSC and SC models reveals the major influence of simulating compressive nonlinearity on the predicted deformational behaviour and failure mechanism of these shear walls. If nonlinear compressive behaviour is neglected in these analyses, as the approach adopted in SC model, the ductility and load carrying capacity are significantly overestimated.

3.5 Parametric study for the model parameters, and mesh sensitivity analysis

A parametric study is executed to assess the influence of the values of the model parameters on the simulated behaviour of the structures analyzed in the previous sections. The parameters under consideration are the compressive strength

(f_c), strain at compressive strength (ε_{c1}), compressive fracture energy ($G_{f,c}$), tensile strength (f_{ct}), and fracture energy mode I (G_f^{I}), that they all have the most significant impact on the predictive performance of the model. To assess the influence of the parameters f_c, ε_{c1}, $G_{f,c}$, f_{ct}, G_f^{I} on the responses predicted by the PDSC model, the values of these parameters are modified from those used in the previous sections (the values of all the remaining parameters were maintained the same as those of Table 1). A mesh analysis is also performed to investigate the the sensitivity of the structural response of the PDSC model to the applied mesh schemes. The RC shear wall S4 was selected for the parametric study and the mesh analysis, but the conclusions to be extracted can be generalized to other structural members simulated in the present work.

3.5.1 Influence of f_c

Fig. 17(a) demonstrates the influence of the concrete compressive strength on the force-deflection (F_h-U_h) relationship when simulating the S4 shear wall (details are provided in Section 3.4). Three different values for f_c were adopted, 20, 30 and 40 N/mm^2, the first one is lower than the value considered in the analysis of Section 3.4 (f_c=30 N / mm^2), while the third is higher. As expected, by increasing f_c the stiffness and the load carrying capacity also increase, but the displacement at peak load is almost the same for the three considered values. As also expected, the F_h-U_h response obtaining using the SC model can be considered an upper limit, since in this model the effect of the nonlinear compressive deformation of concrete is neglected.

The stages where the effect of inelastic compressive deformation becomes relevant on the F_h-U_h responses of the panel in analysis are indicated in Fig. 17(a) using markers. It is verified that these markers are localized in the force-deflection response of the wall when predictions with the PDSC model start diverging from that of SC model. The higher is the concrete compressive strength the larger is the load carrying capacity of the beam corresponding to the marker, which is justified by the adoption of a constant value for the α_0 parameter, which defines the initiation of the inelastic deformation of concrete in compression ($f_{c0} = \alpha_0 f_c$).

3.5.2 Influence of ε_{c1}

The parameter ε_{c1} influences both plasticity and damage parts of the PDSC model. Within the plasticity part, the value of the hardening parameter at compressive strength, $\tilde{\epsilon}_{c1}$, is calculated according to Eq. (7) by attributing a certain value to ε_{c1}. According to this equation $\tilde{\epsilon}_{c1}$ decreases with ε_{c1}, resulting a stiffer pre-peak branch (hardening phase) of the $\bar{\sigma}_c - \tilde{\epsilon}_{c1}$ diagram, as shown in Fig. 3(a).

According to the approach adopted in PDSC model, the damage threshold is assumed to be related to $\tilde{\epsilon}_{c1}$: when $\tilde{\epsilon}_c \leq \tilde{\epsilon}_{c1}$, $d_c = 0$, while for $\tilde{\epsilon}_c > \tilde{\epsilon}_{c1}$ the scalar damage parameter is $d_c > 0$. Therefore by increasing ε_{c1} the $\tilde{\epsilon}_{c1}$ also increases, and the occurrence of damage (i.e. $d_c > 0$), which characterize the entrance of concrete in its compressive strain softening stage, initiates at higher compressive deformation. To assess the influence of the parameter ε_{c1} on the response of the wall in analysis, three values were considered, 0.0018, 0.0035 and 0.0055, the first one is lower than the value considered in the analysis executed in Section 3.4 ($\varepsilon_{c1} = 0.0035$), while the third value is higher. Fig. 17(b) shows that by increasing the ε_{c1} the stiffness of the load vs. deflection response decreases, but the peak load, and mainly its deflection increase, with benefits in terms of the ductility response and load capacity of the beam. In fact by increasing ε_{c1}, in spite of the less stiffer pre-peak branch of the $\bar{\sigma}_c - \tilde{\epsilon}_c$ diagram, the entrance in the concrete compressive strain softening phase (damage activation) is postponed resulting higher deformability and load capacity for the concrete element.

3.5.3 Influence of $G_{f,c}$

The parameter of compressive fracture energy ($G_{f,c}$) controls the rate of strain softening, i.e. the level of stress decrease with the increase of strain, in post-peak stage of the concrete behaviour in compression (see Fig. 3(c)). As larger is $G_{f,c}$ as smaller is this stress decay, which is a characteristic of very ductile materials like fibre reinforced concrete [31].

Fig. 17(c) compares the F_h-U_h responses obtained for three different values of the $G_{f,c}$, 20, 30 and 40 N/mm, the first one is lower than the value considered in the analysis of Section 3.4 ($G_{f,c} = 30$ N/mm), while the third is higher. As can be seen at Fig. 17(c) the parameter $G_{f,c}$ influences the F_h-U_h response of the wall only after the deflection of 7 mm corresponding to the stage that the effect of post-peak strain softening behaviour of concrete under compression becomes relevant. For the deformations larger than 7 mm, the load carrying capacity and ductility of the simulated F_h-U_h curves increase with $G_{f,c}$.

3.5.4 Influence f_{ct}

Fig. 18(a) represents the influence concrete tensile strength (f_{ct}) on the force-deflection (F_h-U_h) relationship of the wall S4. Three different values for f_{ct} were chosen, 1.2, 2.2 and 4.2 N/mm^2, the first one is lower and the last one is higher than the value considered in the analysis of Section 3.4 (f_{ct}=2.2 N / mm^2). Fig. 18(a) shows the influence of f_{ct} is mainly resumed to the first stage of the cracking process, by anticipating this process as lower is f_{ct}, with the

consequent decrease of stiffness of the structural response. When the cracking process is stabilized, the influence of f_{ct} was not totally null because the other fracture parameters were considered the same in these analysis, therefore as larger is f_{ct} as smaller is the ultimate normal crack strain, as shown in Fig. 18(b).

3.5.5 Influence of G_f^{I}

Fig. 19(a) compares the force-deflection (F_h-U_h) relationships obtained for three different values of fracture energy mode I (G_f^{I}), 0.08, 0.14 and 0.4 N/mm, the first one is lower and the last one is higher than the value considered in the analysis of Section 3.4 ($G_f^{\mathrm{I}} = 0.14\ \mathrm{N/mm}$). As can be seen in this figure, after crack initiation the load carrying capacity increases with G_f^{I}, but the stiffness of the response of the structure in its crack propagation stage was not significantly affected. The response of the analysis with G_f^{I} of 0.08 and 0.14 N/mm become almost coincident after the yield initiation of the reinforcement because at this stage the cracks in the governing failure zone are completely open (the fracture energy was completely exhausted). In the analysis with G_f^{I} =0.4 N/mm, the load carrying capacity at post-yielding phase was higher than in the other two simulations (G_f^{I} of 0.08 and 0.14 N/mm) due to the post-cracking residual tensile capacity provided by the cracks at this stage (see Fig. 19(b)).

3.5.6 Influence of mesh size

Size of the finite element mesh used in the section 3.4 for the analysis of the wall S4 is refined with a factor of four in order to show the structural response predicted by the PDSC model is not dependent of the adopted mesh refinement. Fig. 20(a) shows the refined mesh adopted for this analysis. Eight-noded serendipity plane stress finite elements with 3×3 Gauss–Legendre IP scheme are adopted. The F_h-U_h relationship predicted by the analysis with the refined mesh is compared in Fig. 20(b) with that of the analysis with the coarse mesh (the one already obtained in section 3.4). From this figure it is verified that sensitivity of the structural response of the PDSC model to the applied mesh schemes is negligible. Both meshes show similar cracking patterns (see Fig. 16 and Fig. 20(c)).

4. CONCLUSION

This study describes a constitutive approach based on combination of a multidirectional fixed smeared crack model to simulate crack initiation and propagation, and a plastic-damage model to account for nonlinear compressive behaviour of material between the cracks. The crack opening process is initiated based on the Rankine tensile criterion, whereas a trilinear softening diagram is used to simulate the crack propagation. The plasticity part of the model accounts for the

development of irreversible strains and volumetric strain in compression, whereas the strain softening and stiffness degradation of the material under compression are controlled by an isotropic strain base damage model.

The constitutive model was implemented in the finite element computer code FEMIX, and its performance was assessed by simulating concrete and RC structures whose failure mechanisms are governed by, simultaneously, cracking and inelastic compressive deformations. The analysis includes splitting tensile test, RC deep beams, and RC shear wall panels submitted to biaxial loading configuration. The model succeeds to predict with high accuracy the deformational and cracking behaviour as well as the experimentally observed failure modes of the simulated structural members. The results of these analysis indicates the robustness and accuracy of the proposed model for simulating concrete and RC structures subjected to multi-axial loading configurations. A parametric study was also performed to assess the sensitivity of the simulations to the values of the model parameters.

ACKNOWLEDGEMENTS

The authors wish to acknowledge the FCT financial support provided by the Portuguese Foundation for Science and Technology in the scope of the SlabSys-HFRC research project, with reference PTDC/ECM/120394/2010.

REFERENCES

[1] Sena-Cruz, J. M., "Strengthening of concrete structures with near-surface mounted CFRP laminate strips", PhD thesis, Department of Civil Engineering, University of Minho, 2004.

[2] Ventura-Gouveia, A., Barros, J.A.O., Azevedo, A.F.M., "Crack constitutive model for the prediction of punching failure modes of fiber reinforced concrete laminar structures", Computers and Concrete, 8(6), 735-755, 2011.

[3] Barros, J.A.O., Baghi, H., Dias, S.J., Ventura-Gouveia, A., A FEM-based model to predict the behaviour of RC beams shear strengthened according to the NSM technique. Engineering Structures, 56, 1192–206, 2013

[4] Weihe, S., Kröplin, B., de Borst, R., "classification of smeared crack models based on material and structural properties", International Journal of Solids Structures, 35(12), 1289-1308, 1998.

[5] Simone, A., "Continuous-discontinuous modelling of failure", Revue Européenne de Génie Civil, 11:7-8, 1069-1085, 2007 (To link to this article: http://dx.doi.org/10.1080/17747120.2007.9692977).

[6] Pereira, E.B., "Processes of Cracking in Strain Hardening in Cementitious Composites", PhD Thesis, University of Minho, Portugal, 2012.

[7] Zhang, J., Li, J., "Investigation into Lubliner yield criterion of concrete for 3D simulation", Engineering Structures, 44, 122–127, 2012.

[8] Carrazedo, R., Mirmiran, A., Hanai, J.B., "Plasticity based stress–strain model for concrete confinement", Engineering Structures, 48, 645–657, 2013.

[9] Poltronieri, F., Piccolroaz, A., Bigoni, D., Romero Baivier, S., "A simple and robust elastoplastic constitutive model for concrete", Engineering Structures, 60, 81–84, 2014.

[10] Omidi, O., Valliappan, S., Lotfi, V., "Seismic cracking of concrete gravity dams by plastic-damage model using different damping mechanisms", Finite Element in Analysis and Design, 63, 80-97, 2013.

[11] Ayhan, B., Jehel, P., Brancherie, D., Ibrahimbegovic, A., "Coupled damage–plasticity model for cyclic loading: Theoretical formulation and numerical implementation", Engineering Structures, 50, 30–42, 2013.

[12] Mazars, J. and Pijaudier-Cabot, G., "Continuum damage theory - application to concrete", Journal of Engineering Mechanics, 115(2), 345-365, 1989.

[13] Grassl, P., Xenos, D., Nystrom, U., Rempling, R. and Gylltoft, K., "CDPM2: A damage-plasticity approach to modelling the failure of concrete", International Journal of Solids and Structures, 50, 3805–3816, 2013.

[14] Gernay, T., Millard, A. and Franssen, J., "A multiaxial constitutive model for concrete in the fire situation: Theoretical formulation", International Journal of Solids Structures, 50, 3659-3673, 2013.

[15] Edalat Behbahani, A., Barros, J. A. O., and Ventura-Gouveia, A., "Plastic-damage smeared crack model to simulate the behaviour of structures made by cement based materials", International Journal of Solids Structures, 73-74, 20-40, 2015.

[16] Soltanzadeh, F., Edalat Behbahani, A., Mazaheripour, H., Barros, J. A. O, "Shear resistance of SFRSCC short-span beams without transversal reinforcements", Composite Structures, 139, 42-61, 2016.

[17] Sena-Cruz, J.M., Barros, J.A.O., Azevedo, A.F.M. and Ventura-Gouveia, A., "Numerical simulation of the nonlinear behaviour of RC beams strengthened with NSM CFRP strips", Proceedings of CMNE/CILAMCE Congress, FEUP, Porto, Portugal, June, 2007.

[18] de Borst, R., and Nauta, P., "Non-orthogonal cracks in a smeared finite element model", Engineering Computations, 2, 35-46, 1985.

[19] Barros J.A.O., Costa I.G., Ventura-Gouveia A. "CFRP flexural and shear strengthening technique for RC beams: experimental and numerical research", Advances in Structural Engineering Journal, 14(3), 559-581, 2011.

[20] Willam, K. J. and Warnke, E.P., "Constitutive model for the triaxial behaviour of concrete in Concrete Structures Subjected to Triaxial Stresses.", volume 19 of IABSE Report, International Association of Bridge and Structural Engineers, Zurich, pp: 1-30, 1974.

[21] Lee, J., Fenves, J., "A return-mapping algorithm for plastic-damage models: 3-D and plane stress formulation", International Journal for Numerical Methods in Engineering, 50, 487-506, 2001.

[22] CEB-FIP. (2010). *Model Code 2010*: Tomas Telford, Lausanne, Switzerland.

[23] Abrishambaf, A., Barros, J.A.O., Cunha, V.M.C.F, "Relation between fibre distribution and post-cracking behaviour in steel fibre reinforced self-compacting concrete panels", Cement and Concrete Research, 51, 57–66, 2013.

[24] Abrishambaf, A., Barros, J.A.O., Cunha, V.M.F.C., "Tensile stress-crack width law for steel fibre reinforced self-compacting concrete obtained from indirect (splitting) tensile tests", Cement and Concrete Composites, 57:153–165, 2015.

[25] Abrishambaf, A., "Creep behaviour of cracked steel fibre reinforced self-compacting concrete laminar structures", PhD thesis, Department of Civil Engineering, University of Minho, 2015.

[26] Cunha, V.M.C.F, Barros, J.A.O., Sena-Cruz, J.M., "A finite element model with discrete embedded elements for fibre reinforced composites", Computers and Structures, 94-95, 22-33, 2012.

[27] El-Maaddawy, T.A, Sherif, S., "FRP composites for shear strengthening of reinforced concrete deep beams with openings", Composite Structures, 89, 60–69, 2009.

[28] Hawileh, R.A, El-Maaddawy, T.A, Naser, M.Z., "Nonlinear finite element modelling of concrete deep beams with openings strengthened with externally-bonded composites", Materials and Design, 42, 378-387, 2012.

[29] Maier, J. and Thürlimann, B., "Bruchversuche an Stahlbetonscheiben", IBK Bericht 8003-1, ETH Zürich, Institut für Baustatik und Konstruktion (IBK), Zürich, 1985.

[30] Vonk, R.A., "Softening of concrete loaded in compression", PhD thesis, Eindhoven University of Technology, The Netherlands, 1992.

[31] Barros, J.A.O., Sena-Cruz, J.M., "Fracture energy of steel fibre reinforced concrete", Journal of Mechanics of Composite Materials and Structures, 8(1), 29-45, 2001.

529 **NOTATIONS**

a	height of the openings at the deep beam tests
d_c	scalar describing the amount compressive damage
$\underline{\underline{D}}^e$	linear elastic constitutive matrix
D_n^{cr}	the stiffness modulus correspondent to the fracture mode I
D_t^{cr}	the stiffness modulus correspondent to the fracture mode II
E	elasticity modulus of concrete
E_s	unloading-reloading slop for the steel constitutive law
f_c	compressive strength of concrete
f_{ct}	tensile strength of concrete
$f(\underline{\bar{\sigma}}, \bar{\sigma}_c)$	yield function of the plasticity model
f_{c0}	uniaxial compressive stress at plastic threshold
F	applied load (total load) at the splitting tensile test
F_v	initial vertical load applied to the shear wall panel
F_h	horizontal load applied to the shear wall panel
$F_{h,u}^{\exp}$	experimental horizontal load at peak stage of F_h-U_h diagram
$F_{h,u}^{num}$	numerical horizontal load at peak stage of F_h-U_h diagram (predicted by PDSC model)
h	dept of the beam at the deep beam tests
IP	integration point
G_c	elastic shear modulus
G_f^I	mode I fracture energy
$G_{f,c}$	compressive fracture energy
l_b	crack bandwidth
l_c	compressive characteristic length which was assumed identical to the crack bandwidth
n	a generic loading stage of analysis
P	applied load at the deep beam test
P_1	parameter that defines the amount of the decrease of β upon increasing ε_n^{cr}

P_2 parameter that defines the shape of the last branch of the steel stress-strain curve

$P_u^{\exp}$ failure loads of the deep beams at the experimental program

P_u^{num} failure loads of the deep beams obtained by PDSC model

U mid-span deflection at the deep beam test

U_h horizontal deformation of the panel

W crack opening mouth displacement at the splitting tensile test

$\underline{\bar{\sigma}}$ stress vector at global coordinate system providing no compressive damage is included

$\underline{\sigma}$ stress vector at global coordinate system which include compressive damage softening

$\underline{\bar{\sigma}}^{+}$ positive part, tensile, of stress vector $\underline{\bar{\sigma}}$

$\underline{\bar{\sigma}}^{-}$ negative part, compressive, of stress vector $\underline{\bar{\sigma}}$

$\underline{\varepsilon}^{cr}$ crack strain vector

$\underline{\varepsilon}^{co}$ concrete strain vector

$\underline{\varepsilon}$ total strain vector

$\underline{\varepsilon}^{p}$ plastic strain vector

$\underline{\varepsilon}^{e}$ elastic strain vector

σ_n^{cr} normal components of the local crack stress vector

τ_t^{cr} shear components of the local crack stress vector

ε_n^{cr} normal components of the local crack strain vector

γ_t^{cr} shear components of the local crack strain vector

ν Poisson's coefficient

α_i normalized stress parameters (i=1, 2) in the trilinear diagram

β shear retention factor

ξ_i normalized strain parameter (i =1, 2) in the trilinear diagram

$\varepsilon_{n,u}^{cr}$ ultimate crack normal strain

$\bar{\sigma}_c$ hardening function of the plasticity model

ε_{c1} strain at compression peak stress

$\tilde{\epsilon}_c$	compressive hardening variable
$\Delta\lambda$	plastic multiplier
$\tilde{\epsilon}_{c1}$	hardening parameter at uniaxial compressive peak stress
$\tilde{\epsilon}_{cu}$	maximum equivalent strain in compression
α_0	material constant to define the beginning of the nonlinear behaviour in uniaxial compressive stress-strain test
$\tilde{\epsilon}_d$	internal damage variable for compression
θ	crack orientation (angle between the x_1 axis and the vector orthogonal to the plane of the crack)
ρ_x	horizontal reinforcement ratio of web of the shear wall panel
ρ_y	vertical reinforcement ratio of web of the shear wall panel
ρ_F	vertical reinforcement ratio corresponding to the vertical flange of the shear wall panel
$\varepsilon_{sy}, \varepsilon_{sh}, \varepsilon_{su}$	three strain points at the steel constitutive law
$\sigma_{sy}, \sigma_{sh}, \sigma_{su}$	three stress points at the steel constitutive law

Table captions	
Table 1	Values of the parameters of the concrete constitutive model.
Table 2	Details for the deep beam tests.
Table 3	Values of the parameters of the steel constitutive model for deep beams tests.
Table 4	Details for the shear wall panels.
Table 5	Values of the parameters of the steel constitutive model for shear walls tests.

Figure captions	
Fig. 1	Diagram for modelling the fracture mode I at the crack coordinate system [1].
Fig. 2	Relation between crack shear stress and crack shear strain for the incremental approach based on a shear retention factor [19].
Fig. 3	Diagrams for modelling compression: (a) the $\bar{\sigma}_c - \tilde{\epsilon}_c$ relation used in the plasticity model; (b) the $(1-d_c) - \tilde{\epsilon}_d$ relation adopted in the isotropic damage model; (c) the $\sigma_c - \tilde{\epsilon}_c$ diagram for compression with indication of the compressive fracture energy, $G_{f,c}$.
Fig. 4	Details of the splitting tensile test: (a) setup of the test [23]; (b) geometry of the specimen, dimensions are in mm; (c) experimental crack pattern at the failure stage [24].
Fig. 5	Finite element mesh, load and support conditions used for analysis of the splitting tensile test.
Fig. 6	Experimental load vs. crack mouth opening displacement relationship [22] in comparison with the predictions of the PDSC and SC models.
Fig. 7	Predictions of PDSC model for the splitting tensile test: (a) numerical crack pattern; (b) numerical plastic zone (results of (a) and (b) correspond to $W \approx 1.9$ mm, the final converged loading step). Note: In pink color: crack completely open; in red color: crack in the opening process; in cyan color: crack in the reopening process; in green color: crack in the closing process; in blue color: closed crack; in red circle: the plastic zone.
Fig. 8	Deep beams with openings tested by Maaddawy and Sherif [26]: (a) details of the reinforcement system, common for all the beams in the experimental program; (b) geometry of the beams at *group B*, NS-200-B and NS-250-B; (c) geometry of the beams at *group T*, NS-200-T and NS-250-T; (d) geometry of the beams at *group C*, NS-200-C and NS-250-C.
Fig. 9	Finite element mesh, load and support conditions used for analysis of the beam NS-200-C.
Fig. 10	Uniaxial constitutive model (for both tension and compression) for the steel bars [1].
Fig. 11	Experimental load vs. mid-span deflection [26] in compare with the predictions of the PDSC and SC models for the beams: (a) NS-200-B; (b) NS-200-T; (c) NS-200-C; (d) NS-250-B; (e) NS-250-T; (f) NS-250-C.
Fig. 12	Experimental crack patterns [26] for the beams: (a) NS-200-B; (b) NS-200-T; (c) NS-250-B; (d) NS-250-T; (e) NS-250-C.
Fig. 13	Numerical crack patterns (left) and plastic zones (right) predicted by PDSC model for the beams in analysis (the results correspond to the final converged step).

	Note: the crack pattern and plastic zone are represented over the finite element mesh adopted for the concrete.
Fig. 14	Geometry and loading configurations of the shear walls tested by Maier and Thürlimann [28] (dimensions in mm): (a) the walls in *group A* (with vertical flange); (b) the walls in *group B* (without vertical flange).
Fig. 15	Simulation of the S3 shear wall tested by Maier and Thürlimann [28]: (a) finite element mesh used for the analysis; (b) horizontal load vs. horizontal displacement relationship, F_h-U_h; (c) numerical crack pattern predicted by PDSC model and (d) plastic zone predicted by PDSC model (results of (c) and (d) correspond to $U_h \approx 16.5 mm$, the final converged step); (e) experimentally observed crack pattern [28]. Note: the crack pattern and plastic zone are represented over the finite element mesh adopted for the concrete.
Fig. 16	Simulation of the shear walls S1, S2, S4, S9, S10 tested by Maier and Thürlimann [28]: (a) horizontal load versus horizontal displacement relationship, F_h-U_h; (b) numerical crack pattern predicted by PDSC model and corresponding to the final converged step; (c) experimentally observed crack pattern [28]. Note: the crack pattern is represented over the finite element mesh adopted for the concrete.
Fig. 17	Sensitivity of the analysis of the panel S4 respect to the values of the parameters: (a) f_c; (b) ε_{c1}; (c) $G_{f,c}$.
Fig. 18	Sensitivity of the analysis of the panel S4 respect to the value of the parameter f_{ct}: (a) F_h-U_h relationship; (b) crack normal stress-crack normal strain diagram ($\sigma_n^{cr} - \varepsilon_n^{cr}$) for the f_{ct} equal to 1.2, 2.2, and 4.2 MPa.
Fig. 19	Sensitivity of the analysis of the panel S4 respect to the value of the parameter fracture energy mode I (G_f^{I}): (a) F_h-U_h relationship; (b) crack normal stress-crack normal strain diagram ($\sigma_n^{cr} - \varepsilon_n^{cr}$) for the G_f^{I} equal to 0.08, 0.14, and 0.4 MPa.
Fig. 20	Sensitivity of the analysis of the panel S4 respect to the size of finite element mesh: (a) refined finite element mesh used for analysis; (b) F_h-U_h relationship; (c) Numerical crack pattern obtained at final converged step of the analysis. Note: the crack pattern is represented over the finite element mesh adopted for the concrete.

573

574

575 Table 1 – Values of the parameters of the concrete constitutive model.

Property	Value
Poisson's ratio	$\nu = 0.2$
Young's modulus	for the splitting tensile test $E = 36000\,N/mm^2$; for the deep beam tests $E = 20000\,N/mm^2$; for the shear wall tests $E = 26000\,N/mm^2$;
Parameters defining the plastic-damage part of the model	for the splitting tensile test $f_c = 48.0\,N/mm^2; G_{f,c} = 35.0\,N/mm;\ \varepsilon_{c1} = 0.0035$; for the deep beam tests $f_c = 20.0\,N/mm^2; G_{f,c} = 8.0\,N/mm;\ \varepsilon_{c1} = 0.0035$; for the shear wall tests $f_c = 30.0\,N/mm^2; G_{f,c} = 30.0\,N/mm;\ \varepsilon_{c1} = 0.0035$;
Parameter to define elastic limit state	for all the simulations $\alpha_0 = 0.4$
Parameter defining the Trilinear tension-softening diagram	for the splitting tensile test $f_{ct} = 3.5\,N/mm^2; G_f^{\mathrm{I}} = 3.0\,N/mm; \xi_1 = 0.007; \alpha_1 = 0.5; \xi_2 = 0.15; \alpha_2 = 0.55$; for the deep beam tests $f_{ct} = 1.1\,N/mm^2; G_f^{\mathrm{I}} = 0.04\,N/mm; \xi_1 = 0.0022; \alpha_1 = 0.3; \xi_2 = 0.1; \alpha_2 = 0.15$; for the shear wall tests $f_{ct} = 2.2\,N/mm^2; G_f^{\mathrm{I}} = 0.14\,N/mm; \xi_1 = 0.15; \alpha_1 = 0.3; \xi_2 = 0.575; \alpha_2 = 0.15$;
Parameter defining the mode I fracture energy available to the new crack [1]	for all the simulations 2
Type of shear retention factor law	for all the simulations $P_1 = 2$
Crack bandwidth	for all the simulations this parameter was set as square root of the area of Gauss integration point
Threshold angle [1]	for all the simulations 30 degree
Maximum number of cracks per integration point [1]	for all the simulations 2

576

577

578

579

580

581

582

583

584

585

586

587

588

589

590

591

Table 2 – Details for the deep beam tests.

specimen ID	geometry	opening size (mm^2)	a/h[4] ratio	P_u^{exp} (kN)	P_u^{num} (kN)	$\left\|P_u^{exp} - P_u^{num}\right\| / P_u^{exp}$ (%)
NS-200-B	*group B*[1]	200×200	0.4	210.7	212	0.61
NS-250-B	*group B*	250×250	0.5	137.9	143.15	3.8
NS-200-C	*group C*[2]	200×200	0.4	163	183	12.2
NS-250-C	*group C*	250×250	0.5	106.6	108.9	2.1
NS-200-T	*group T*[3]	200×200	0.4	220	236	7.2
NS-250-T	*group T*	250×250	0.5	127.6	128.6	0.78
					average	4.45

(1) Opening is located at bottom of shear span near loading point.
(2) Opening is located at middle of the shear span.
(3) Opening is located at top of shear span near support.
(4) a: height of openings; h: dept of the beam.

Table 3 – Values of the parameters of the steel constitutive model for deep beams tests.

	$\varepsilon_{sy}(\%)$	$\sigma_{sy}(N/mm^2)$	$\varepsilon_{sh}(\%)$	$\sigma_{sh}(N/mm^2)$	$\varepsilon_{su}(\%)$	$\sigma_{su}(N/mm^2)$	Third branch exponent
$\phi 14$	0.21	420	1.4	430	4.4	540	1
$\phi 8$	0.21	420	1.4	430	4.4	540	1
$\phi 6$	0.15	300	1.4	330	4.4	440	1

Table 4 – Details for the shear wall panels.

Specimen ID	geometry	ρ_x (%)	ρ_y (%)	ρ_F (%)	F_v (kN)	$F_{h,u}^{\exp}$ (kN)	$F_{h,u}^{num}$ (kN)	$\left\|F_{h,u}^{\exp} - F_{h,u}^{num}\right\| / F_{h,u}^{\exp}$ (%)
S1	*group A*	1.03	1.16	1.16	433	680	721	6.0
S2	*group A*	1.03	1.16	1.16	1653	928	958	3.3
S3	*group A*	1.03	2.46	2.46	424	977	991	1.4
S4	*group B*	1.03	1.05	1.05	262	392	364	7.1
S9	*group B*	0.0	0.99	0.99	260	342	310	9.3
S10	*group B*	0.98	1.0	5.71	262	670	656	2
							average	4.85

678 Table 5 – Values of the parameters of the steel constitutive model for shear walls tests.

	$\varepsilon_{sy}(\%)$	$\sigma_{sy}(N/mm^2)$	$\varepsilon_{sh}(\%)$	$\sigma_{sh}(N/mm^2)$	$\varepsilon_{su}(\%)$	$\sigma_{su}(N/mm^2)$	Third branch exponent
$\phi 8$	0.287	574	0.287	574	2.46	764	1

679

680

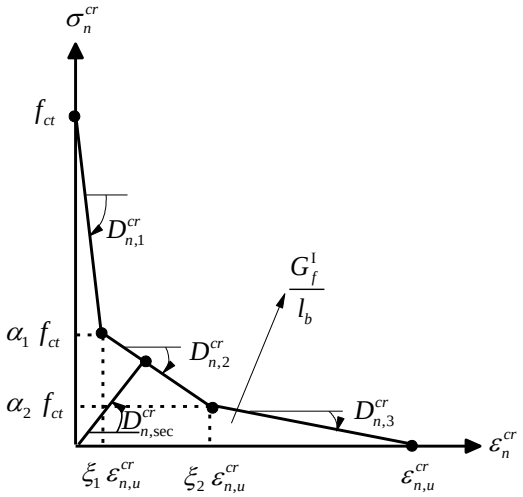

Fig. 1 – Diagram for modelling the fracture mode I at the crack coordinate system [1].

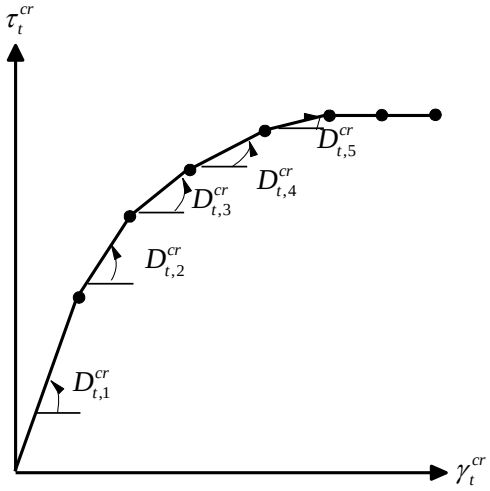

Fig. 2 – Relation between crack shear stress and crack shear strain for the incremental approach based on a shear retention factor [19].

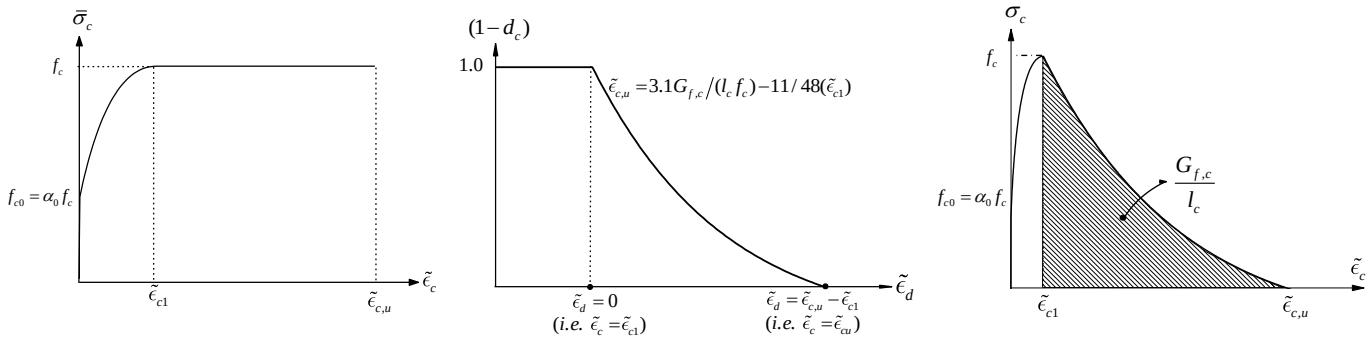

(a) (b) (c)

Fig. 3 – Diagrams for modelling compression: (a) the $\bar{\sigma}_c-\tilde{\epsilon}_c$ relation used in the plasticity model; (b) the $(1-d_c)-\tilde{\epsilon}_d$ relation adopted in the isotropic damage model; (c) the $\sigma_c-\tilde{\epsilon}_c$ diagram for compression with indication of the compressive fracture energy, $G_{f,c}$.

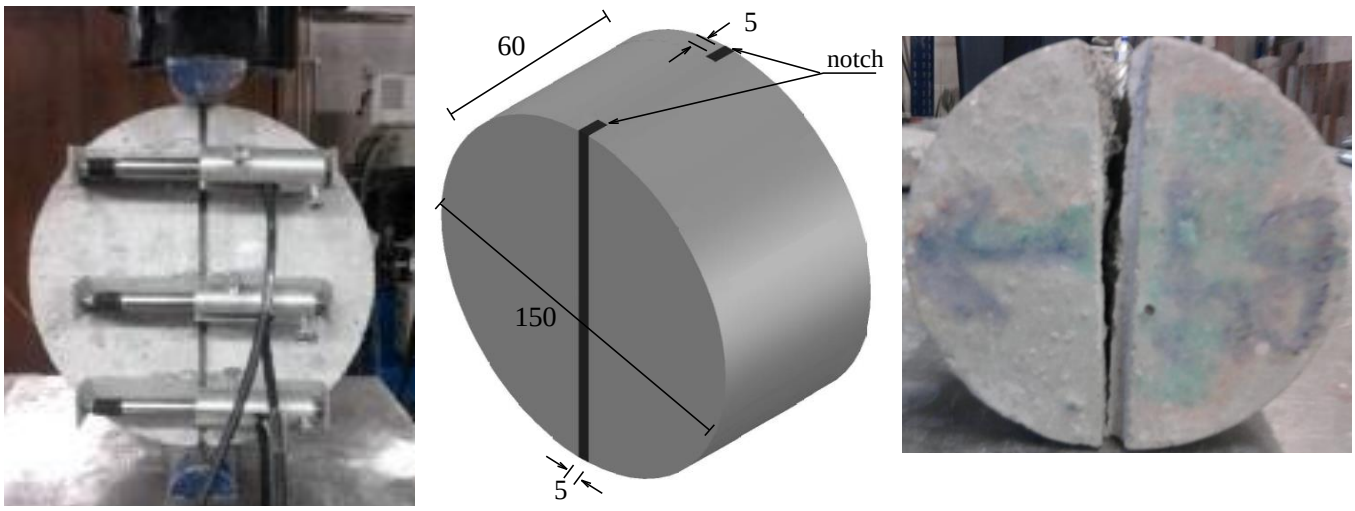

(a) (b) (c)

Fig. 4 – Details of the splitting tensile test: (a) setup of the test [24]; (b) geometry of the specimen, dimensions are in mm; (c) experimental crack pattern at the failure stage [25].

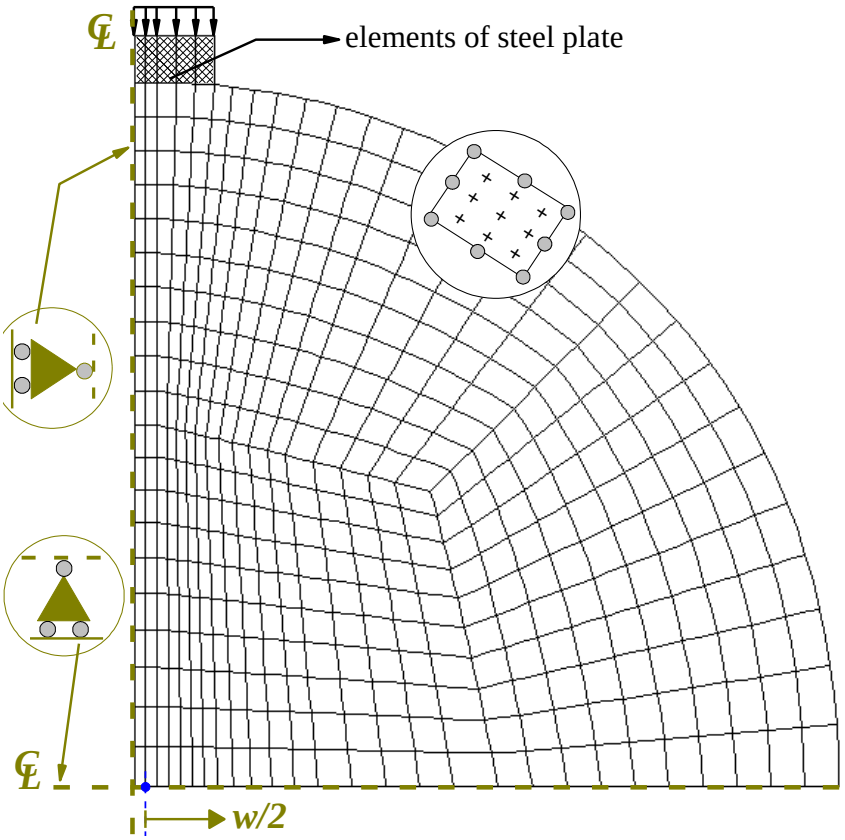

Fig. 5 – Finite element mesh, load and support conditions used for analysis of the splitting tensile test.

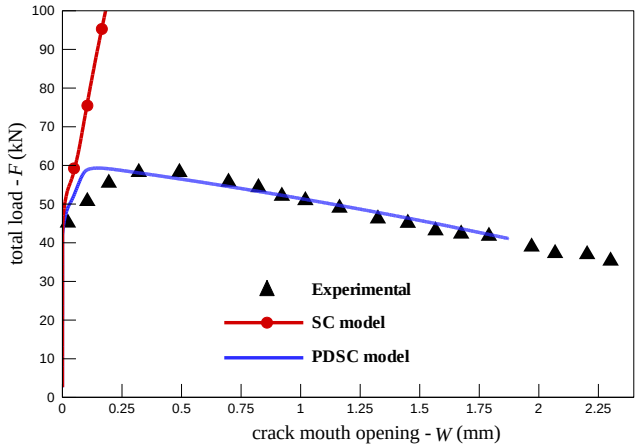

Fig. 6 – Experimental load vs. crack mouth opening displacement relationship [22] in comparison with the predictions of the PDSC and SC models.

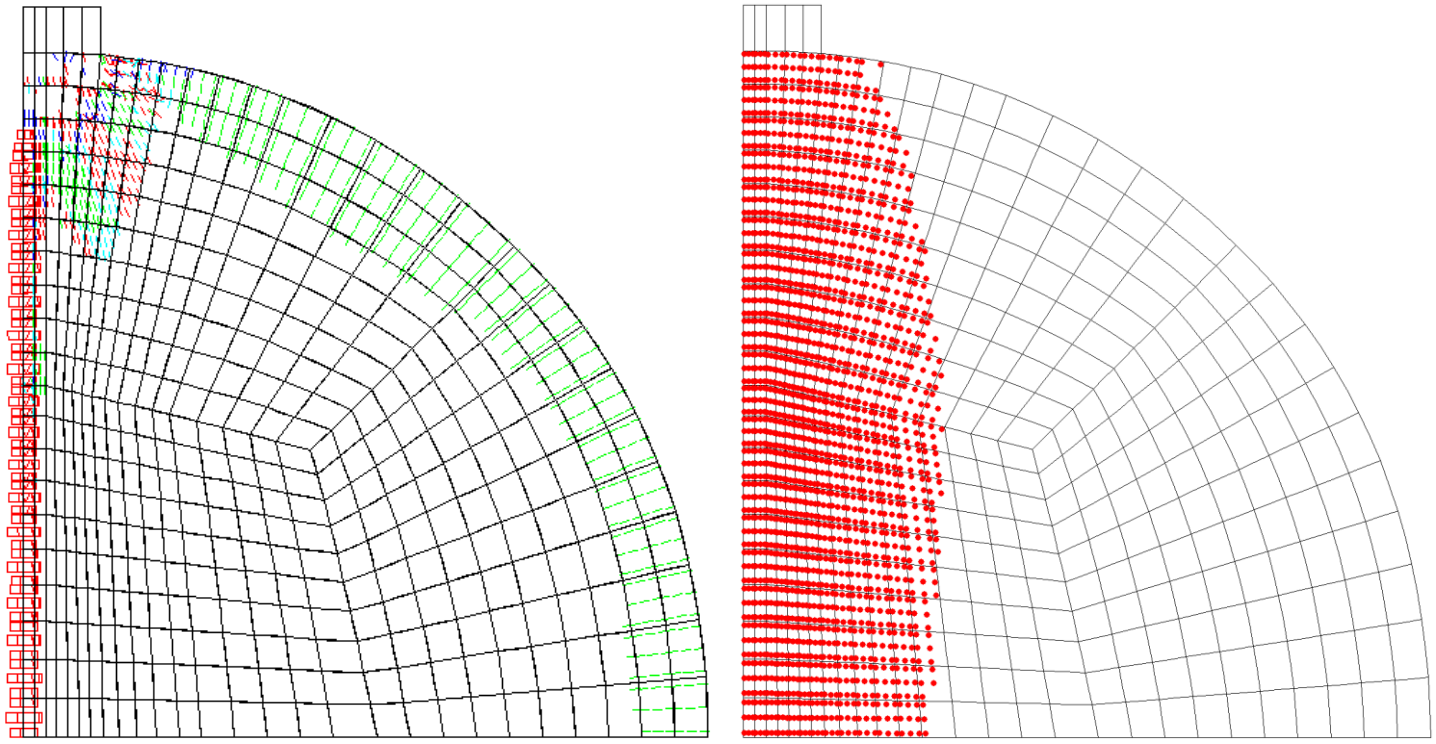

(a) (b)

Fig. 7 – Predictions of PDSC model for the splitting tensile test: (a) numerical crack pattern; (b) numerical plastic zone (results of (a) and (b) correspond to $W \approx 1.9$ mm, the final converged loading step).

Note: In pink color: crack completely open; in red color: crack in the opening process; in cyan color: crack in the reopening process; in green color: crack in the closing process; in blue color: closed crack; in red circle: the plastic zone.

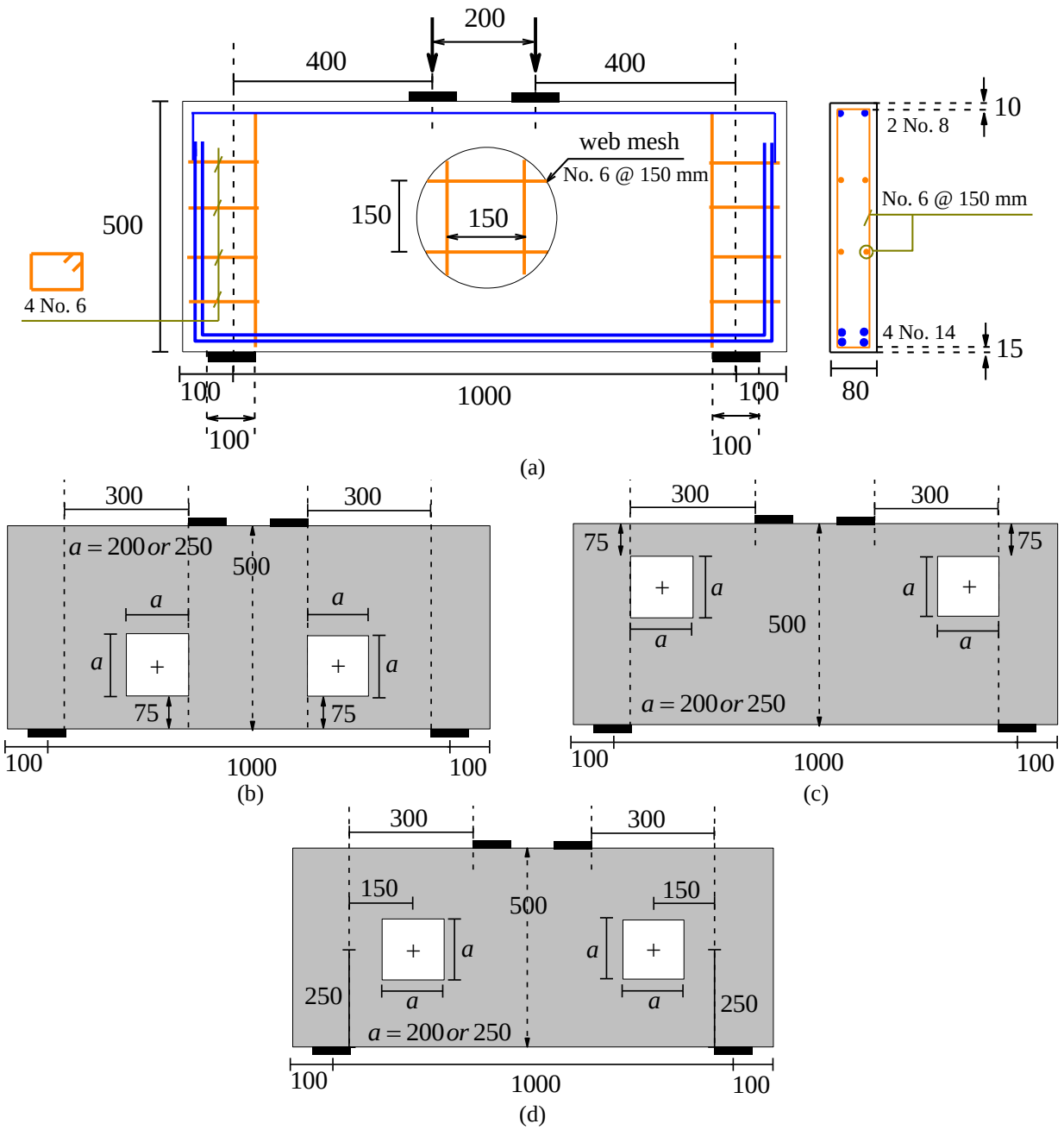

Fig. 8 – Deep beams with openings tested by El-Maaddawy and Sherif [27]: (a) details of the reinforcement system, common for all the beams in the experimental program; (b) geometry of the beams at *group B*, NS-200-B and NS-250-B; (c) geometry of the beams at *group T*, NS-200-T and NS-250-T; (d) geometry of the beams at *group C*, NS-200-C and NS-250-C.

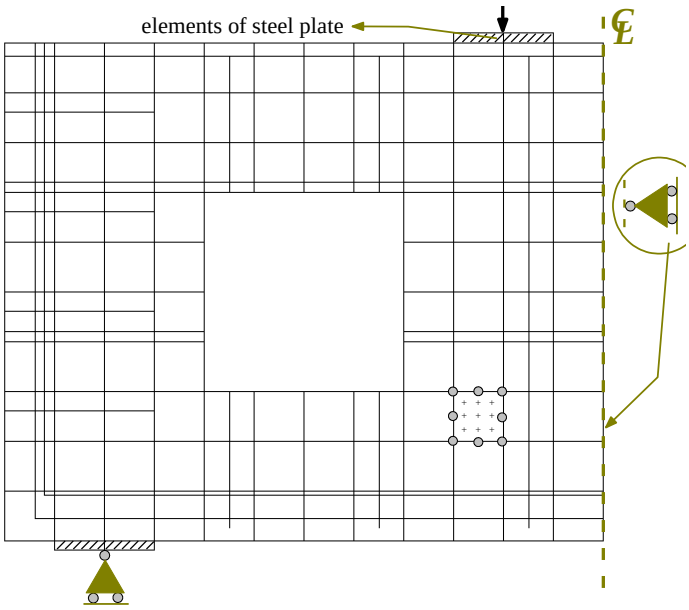

Fig. 9 – Finite element mesh, load and support conditions used for analysis of the beam NS-200-C.

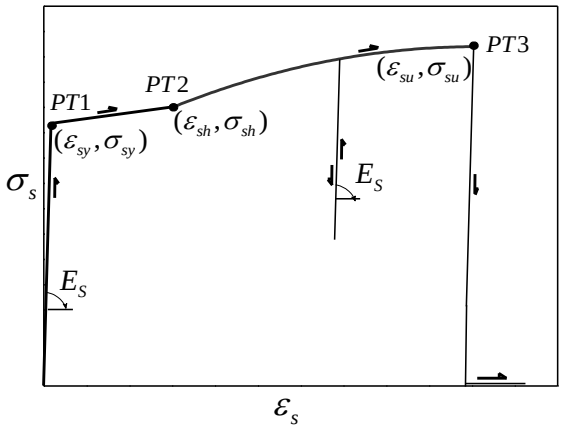

Fig. 10 – Uniaxial constitutive model (for both tension and compression) for the steel bars [1].

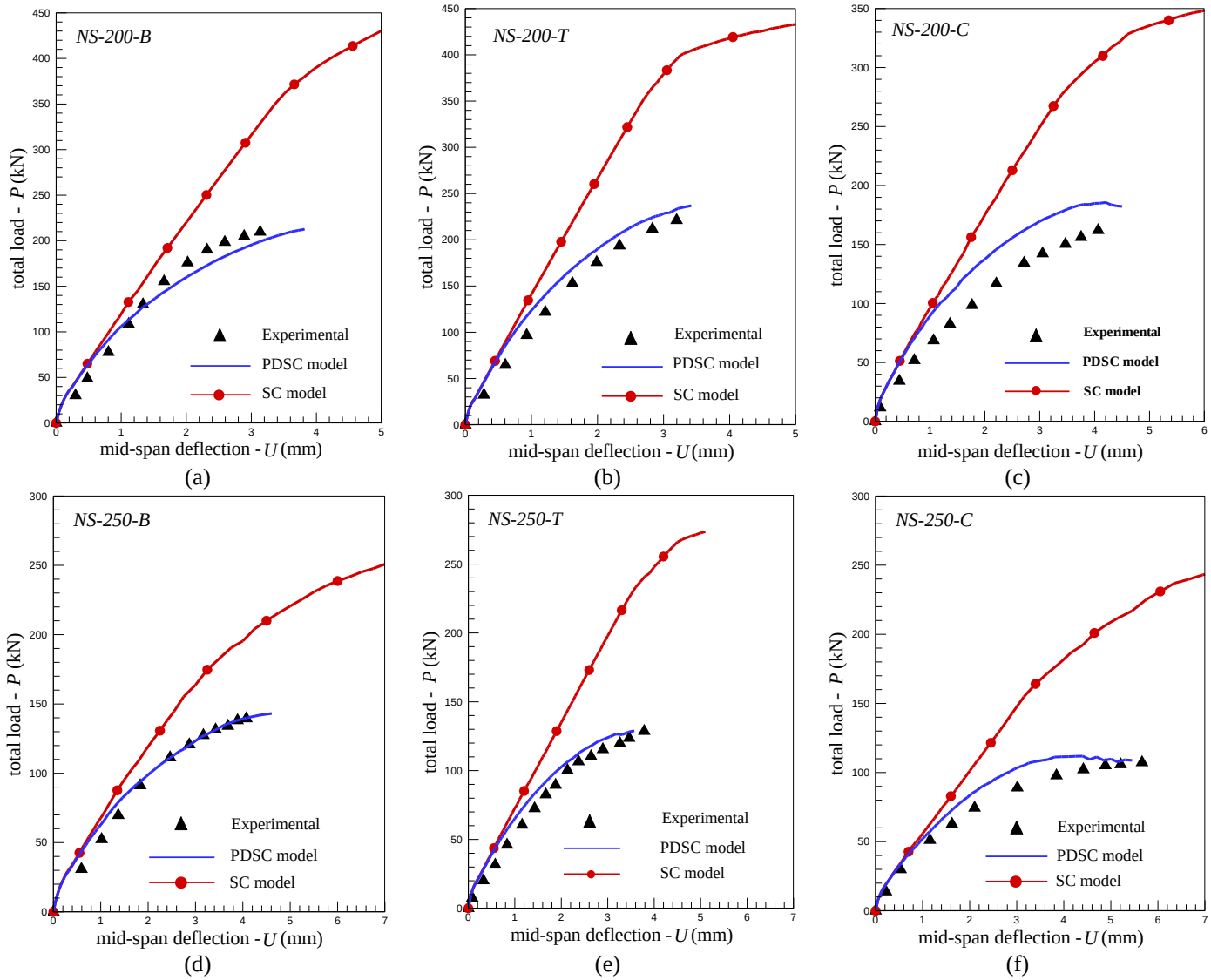

Fig. 11 – Experimental load vs. mid-span deflection [27] in compare with the predictions of the PDSC and SC models for the beams: (a) NS-200-B; (b) NS-200-T; (c) NS-200-C; (d) NS-250-B; (e) NS-250-T; (f) NS-250-C.

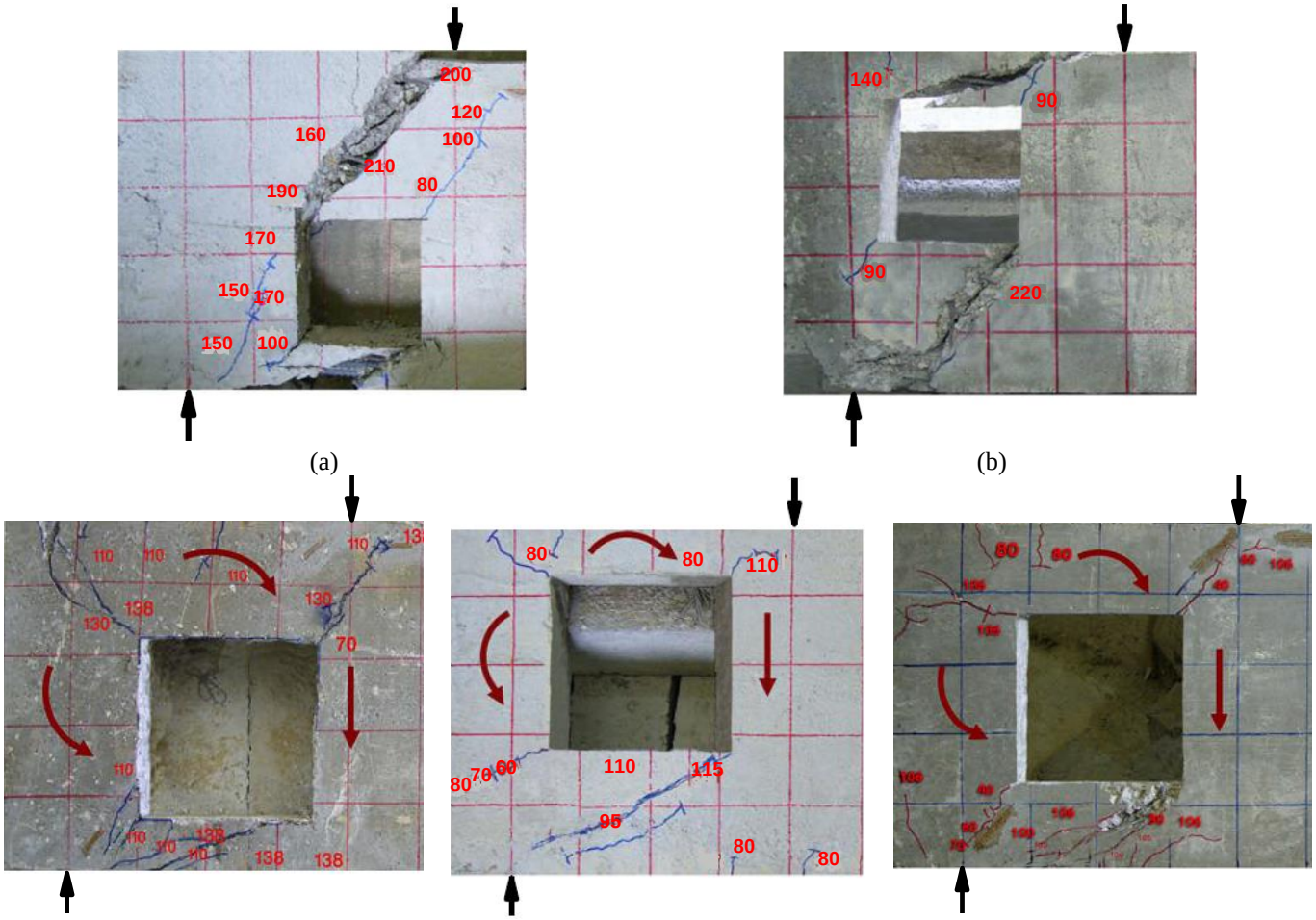

(a) (b)

(c) (d) (e)

Fig. 12 – Experimental crack patterns [27] for the beams: (a) NS-200-B; (b) NS-200-T; (c) NS-250-B; (d) NS-250-T; (e) NS-250-C.

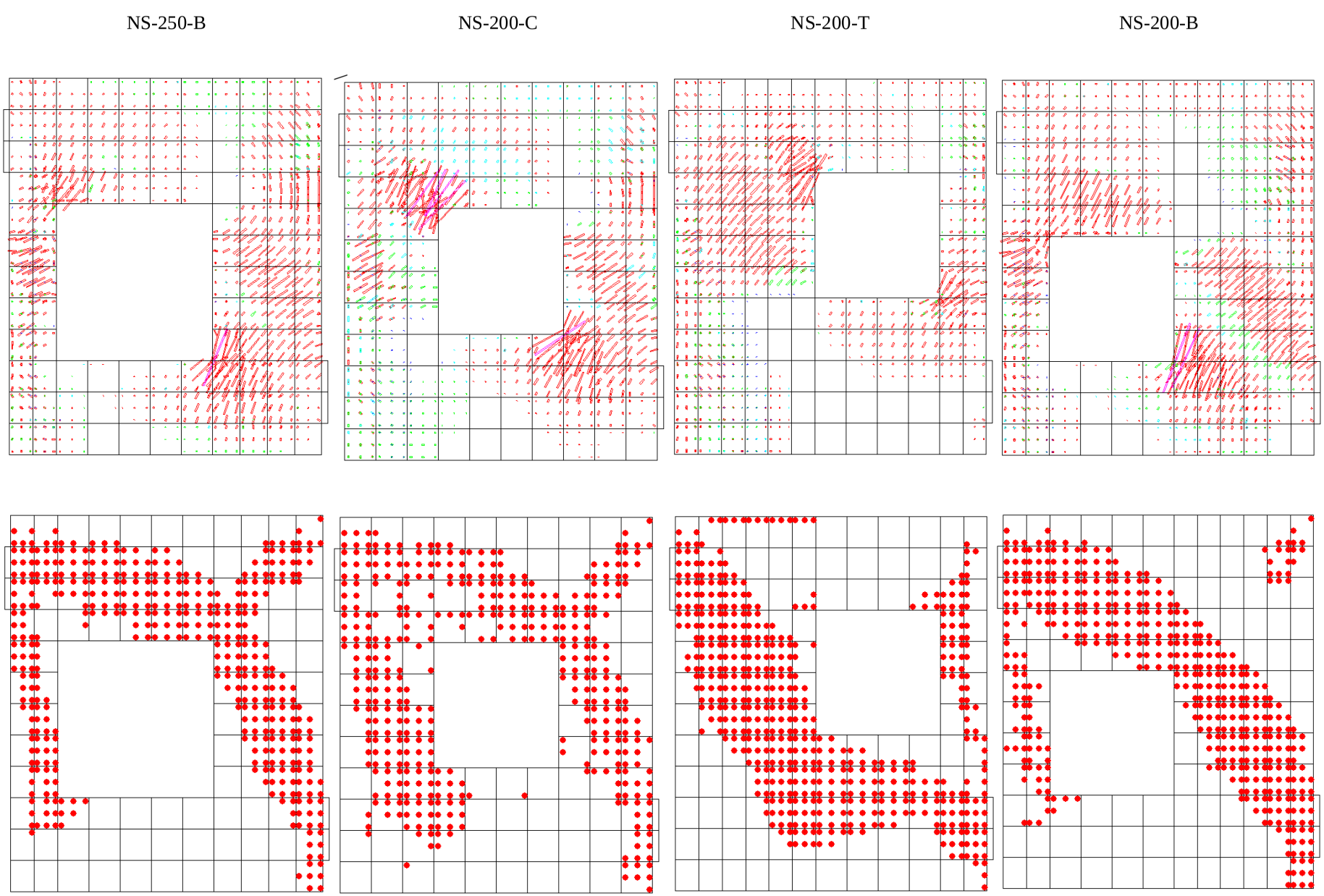
NS-250-B
NS-200-C
NS-200-T
NS-200-B

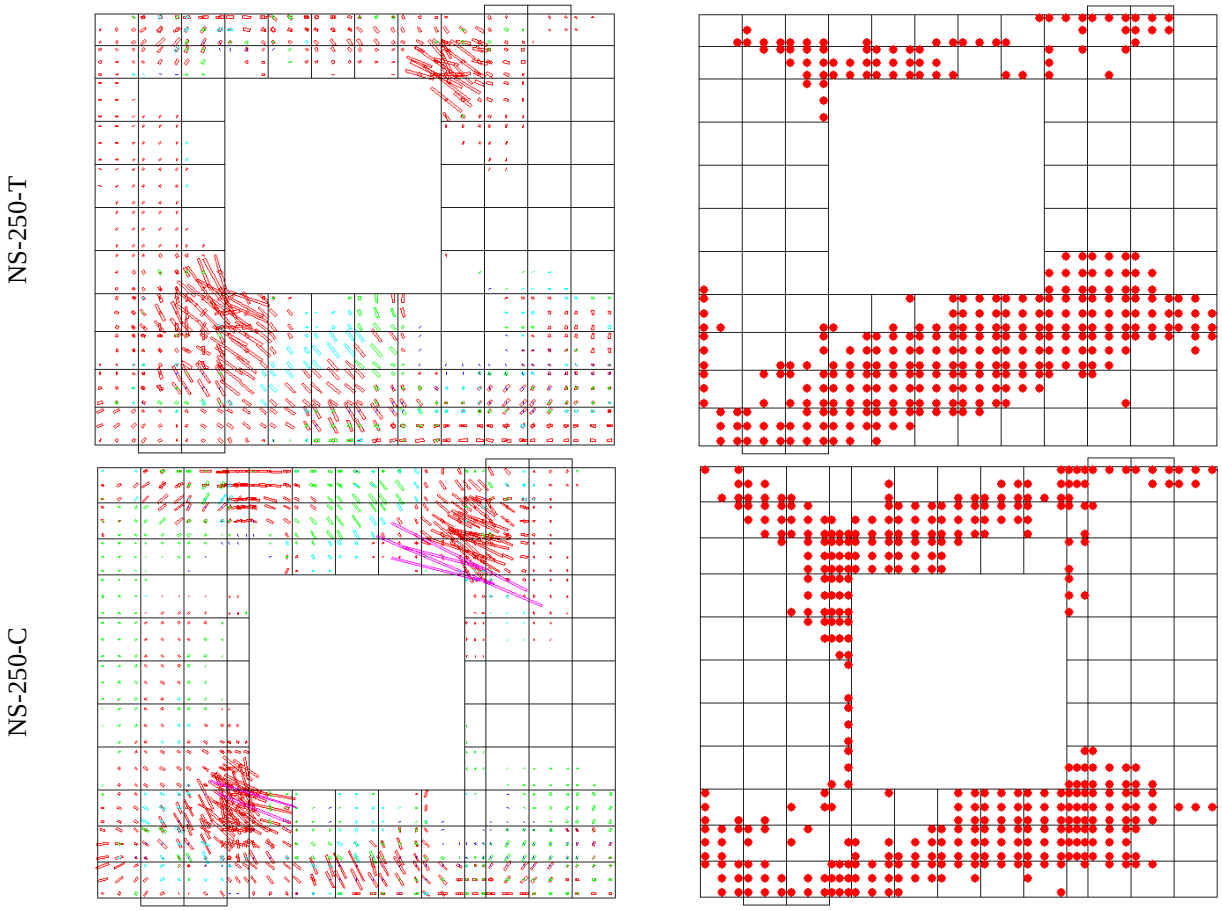

Fig. 13 – Numerical crack patterns (left) and plastic zones (right) predicted by PDSC model for the beams in analysis (the results correspond to the final converged step).
Note: the crack pattern and plastic zone are represented over the finite element mesh adopted for the concrete.

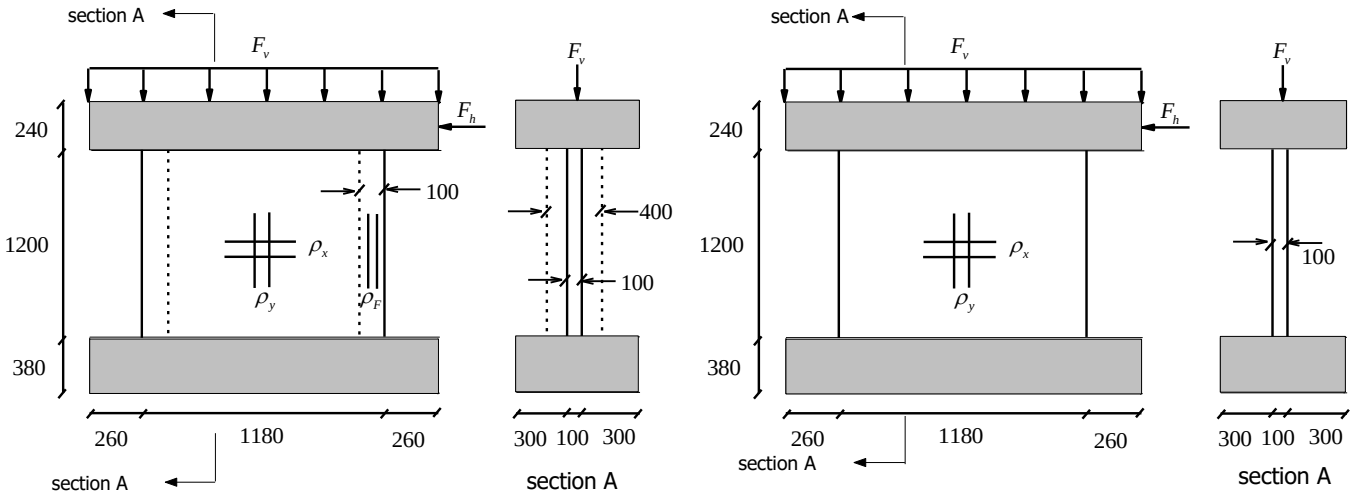

Fig. 14 – Geometry and loading configurations of the shear walls tested by Maier and Thürlimann [29] (dimensions in mm): (a) the walls in *group A* (with vertical flange); (b) the walls in *group B* (without vertical flange).

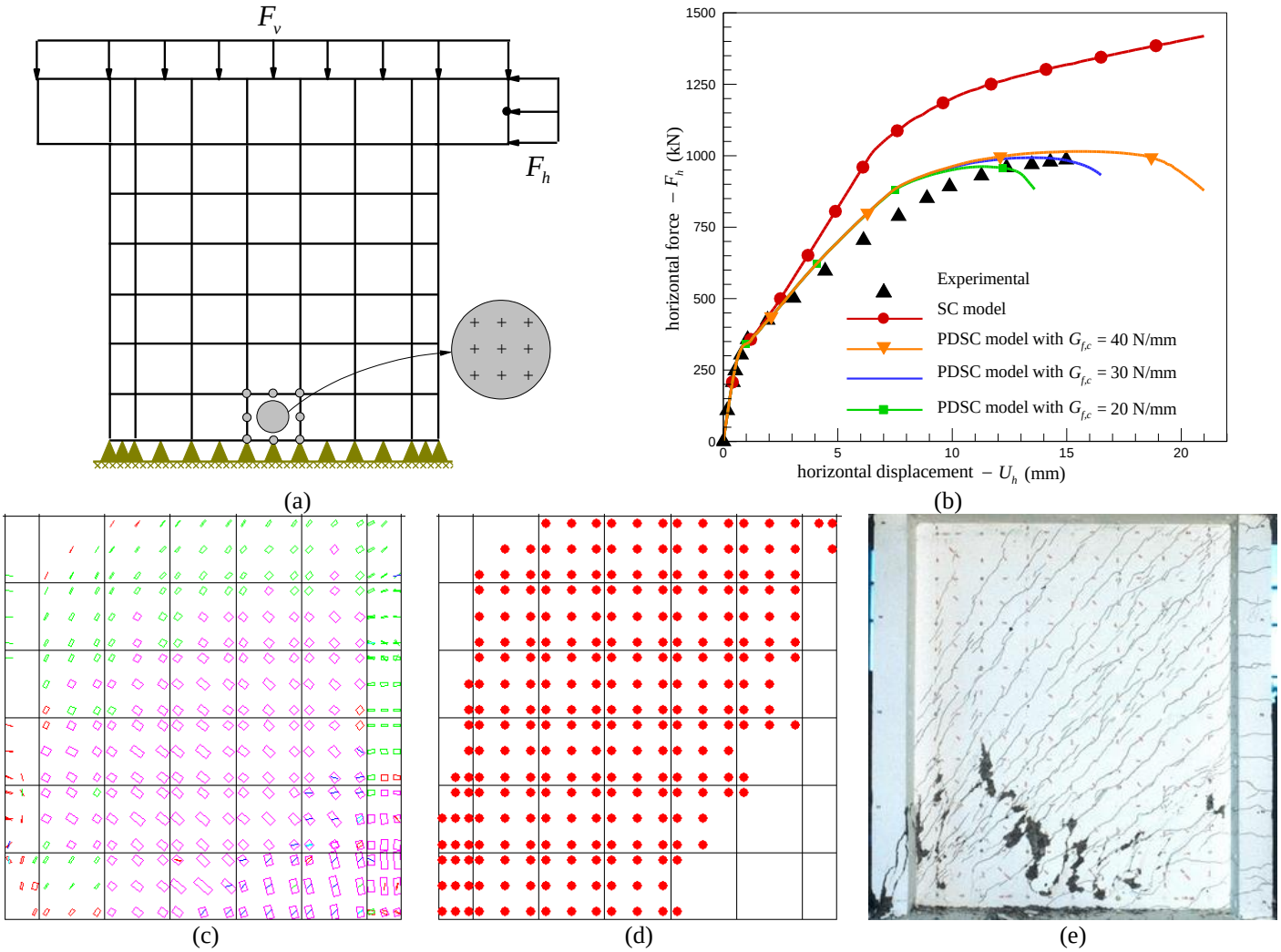

Fig. 15 – Simulation of the S3 shear wall tested by Maier and Thürlimann [29]: (a) finite element mesh used for the analysis; (b) horizontal load vs. horizontal displacement relationship, F_h-U_h; (c) numerical crack pattern predicted by PDSC model and (d) plastic zone predicted by PDSC model (results of (c) and (d) correspond to $U_h \approx 16.5 mm$, the final converged step); (e) experimentally observed crack pattern [29].
Note: the crack pattern and plastic zone are represented over the finite element mesh adopted for the concrete.

panel S1

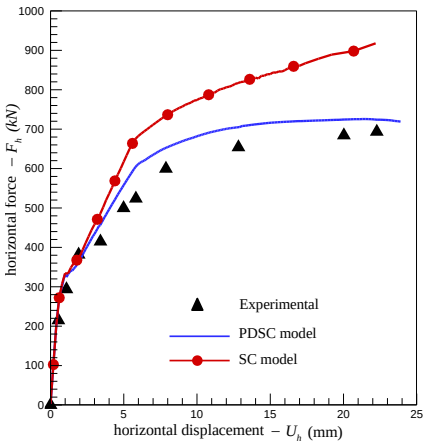

(a)

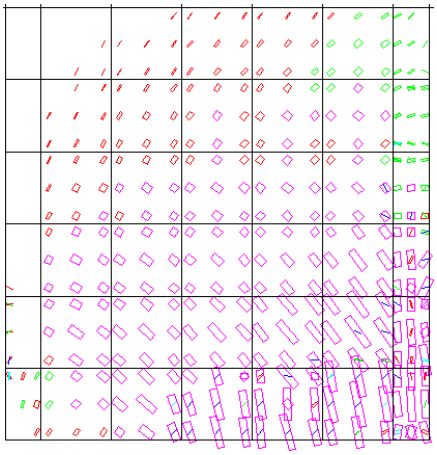

(b)

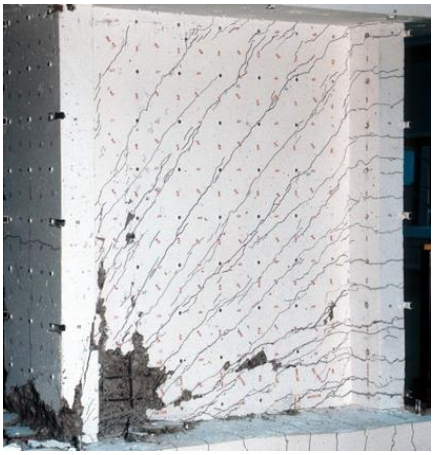

(c)

panel S2

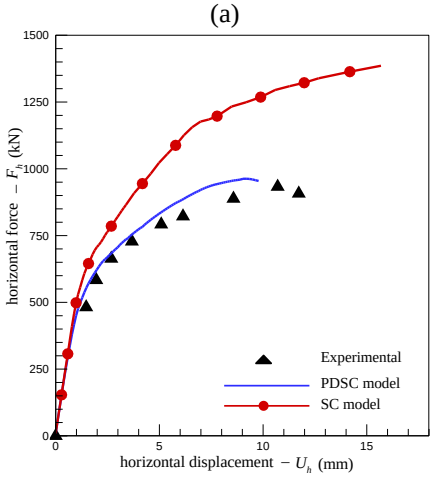

(a)

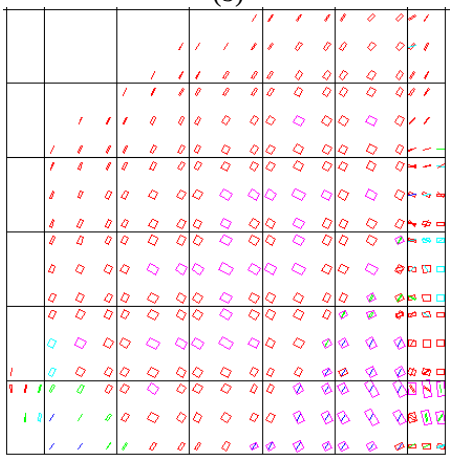

(b)

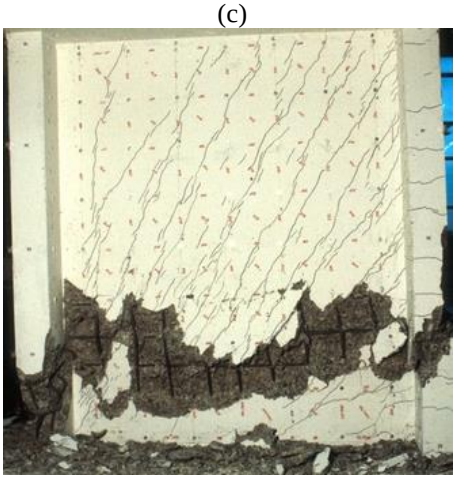

(c)

panel S4

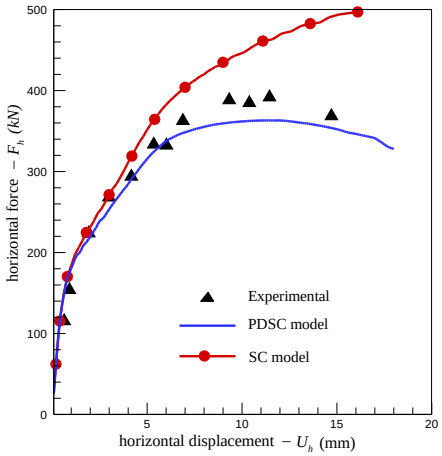

(a)

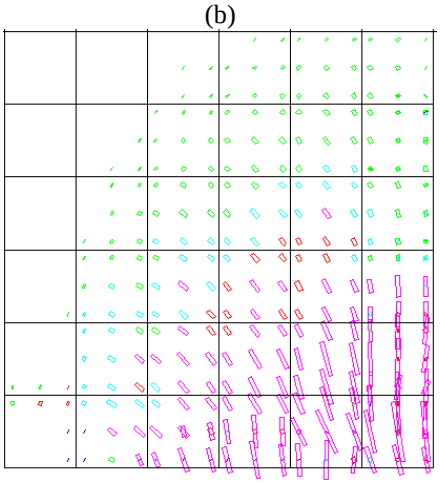

(b)

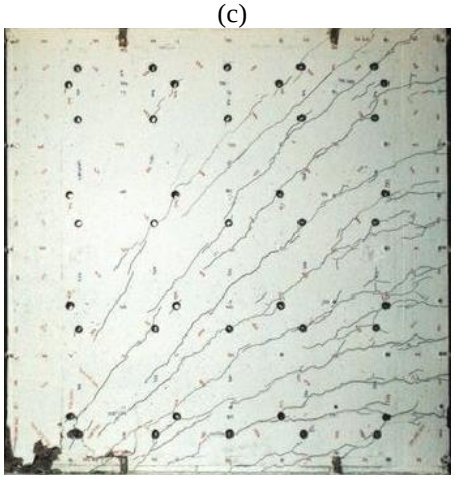

(c)

panel S9

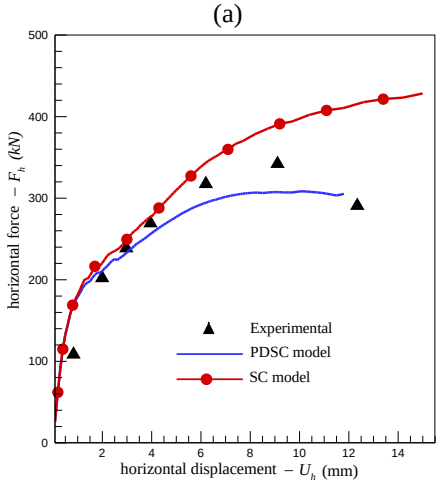

(a)

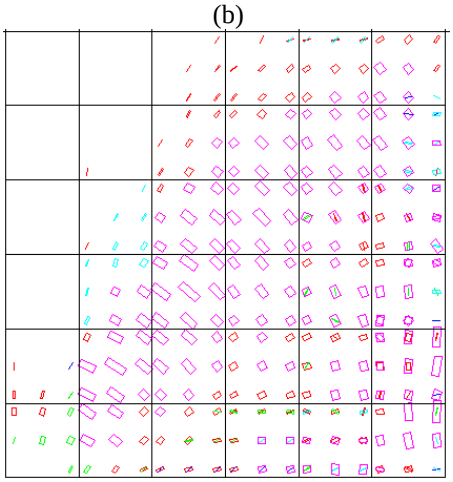

(b)

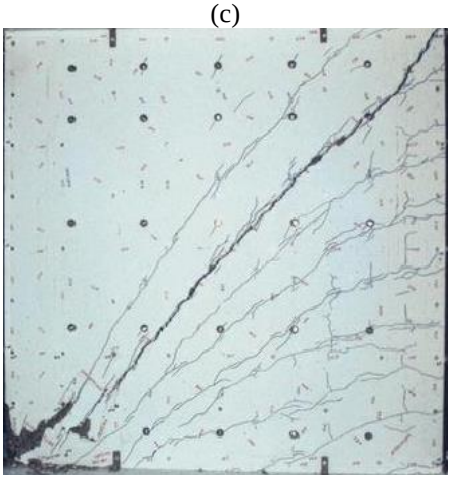

(c)

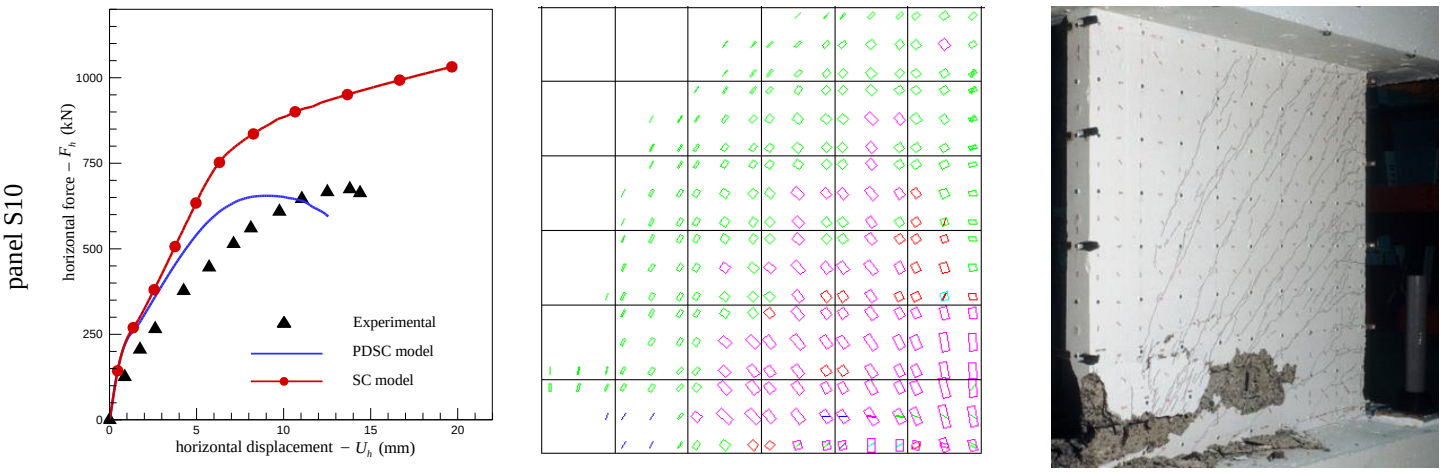

(a) (b) (c)

Fig. 16 – Simulation of the shear walls S1, S2, S4, S9, S10 tested by Maier and Thürlimann [29]: (a) horizontal load versus horizontal displacement relationship, F_h-U_h; (b) numerical crack pattern predicted by PDSC model and corresponding to the final converged step; (c) experimentally observed crack pattern [29].

Note: the crack pattern is represented over the finite element mesh adopted for the concrete.

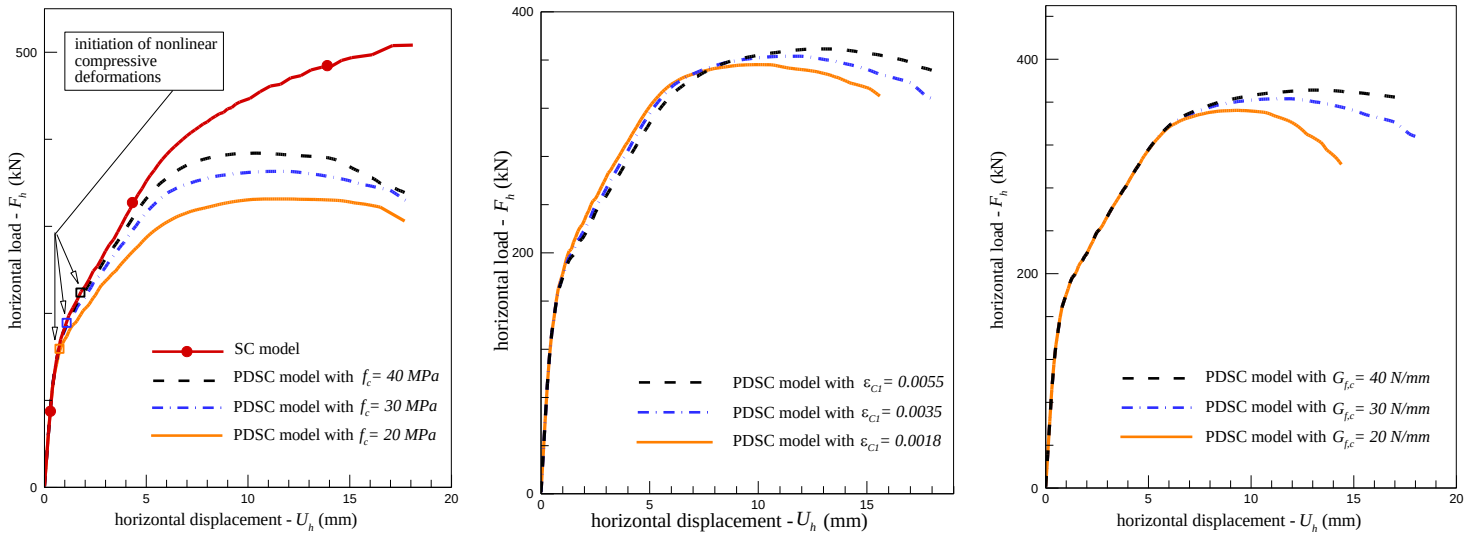

(a) (b) (c)

Fig. 17 – Sensitivity of the analysis of the panel S4 respect to the values of the parameters: (a) f_c ; (b) ε_{c1} ; (c) $G_{f,c}$.

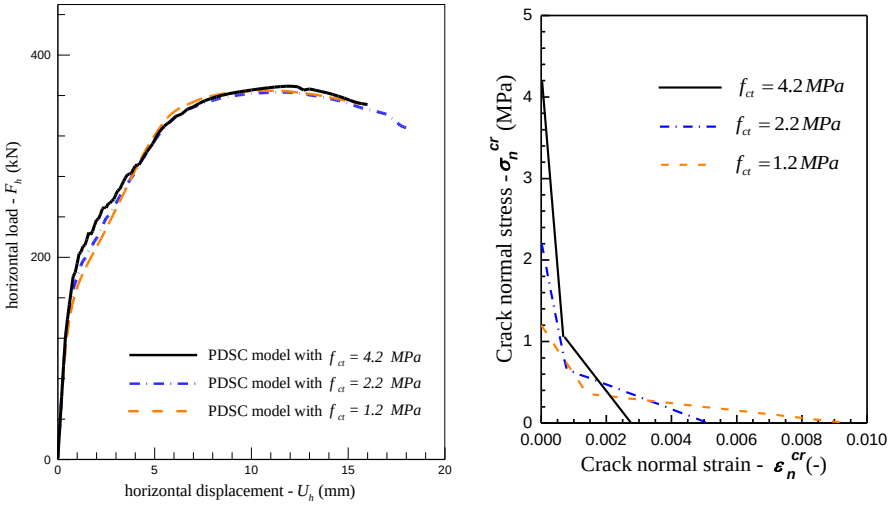

(a) (b)

Fig. 18 – Sensitivity of the analysis of the panel S4 respect to the value of the parameter f_{ct} : (a) F_h-U_h relationship; (b) crack normal stress-crack normal strain diagram ($\sigma_n^{cr} - \varepsilon_n^{cr}$) for the f_{ct} equal to 1.2, 2.2, and 4.2 MPa.

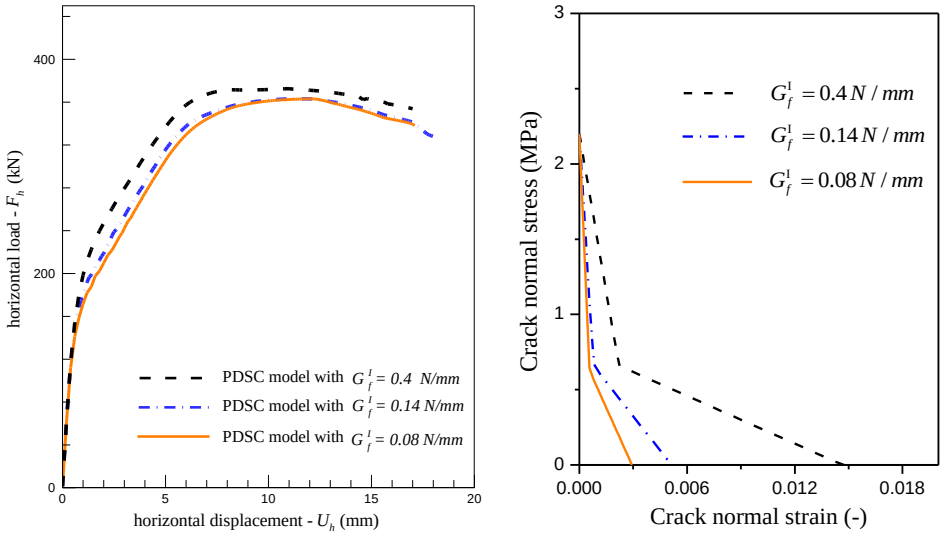

(a) (b)

Fig. 19 – Sensitivity of the analysis of the panel S4 respect to the value of the parameter fracture energy mode I (G_f^I): (a) F_h-U_h relationship; (b) crack normal stress-crack normal strain diagram ($\sigma_n^{cr} - \varepsilon_n^{cr}$) for the G_f^I equal to 0.08, 0.14, and 0.4 MPa.

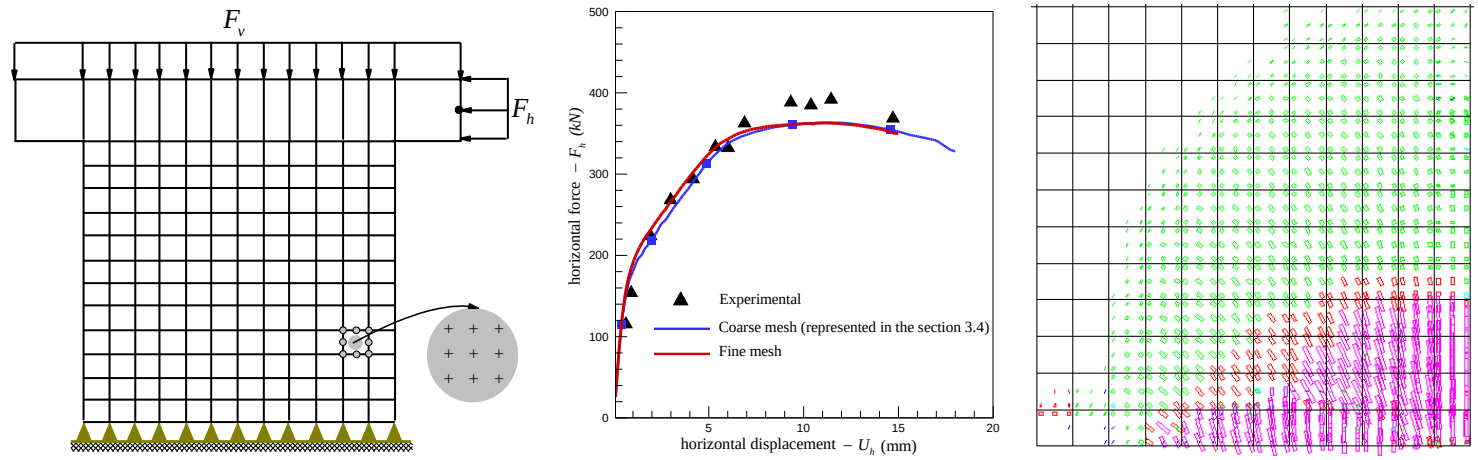

(a) (b) (c)

Fig. 20 – Sensitivity of the analysis of the panel S4 respect to the size of finite element mesh: (a) refined finite element mesh used for analysis; (b) F_h-U_h relationship; (c) Numerical crack pattern obtained at final converged step of the analysis.
Note: the crack pattern is represented over the finite element mesh adopted for the concrete.